

Computation of stress and material property fields from the spatial distribution of strains: physics-based iterative algorithm

N. B. Guerra^a, S. J. C. Matthews^b, S. R. Arwade^c, L. C. M. Vieira Jr.^a, S. Szyniszewski^d

^a*University of Campinas, Brazil*

^b*RINA Tech UK Ltd, United Kingdom*

^c*University of Massachusetts at Amherst, United States*

^d*Durham University, United Kingdom*

Abstract

The present work presents a numerical algorithm for computing the spatial distribution of material properties within a tested sample from known values of the strain field and the applied loading. Quantification of material properties across the specimen is useful for quality control of manufactured parts and health monitoring of ageing structures by locating soft spots or defects. Identification of material property fields also enables stochastic modelling since parameters such as spatial fluctuation scale or cross-correlations between the variables are determined. Our method employs analytical constitutive relationship between measured strains and simulated stresses to update a finite element model. We used virtual experiments with stochastic distributions of material properties for benchmarking. The proposed iterative algorithm converged to stable solutions across a range of stochastic fields (smoothly varying and highly discontinuous). The presented method works with 3D strain data sets (from digital volume correlation, DVC) and 2D fields (from digital image correlation, DIC). We also show that reliable results can be obtained in spite of the presence of random, experimental measurement noise. Future studies can focus on the generalization to hyperelastic, plastic and non-linear material parameters.

1. Introduction

Heterogeneous materials exhibit significant spatial variability due to the presence of multiple phases or base materials as well as their porosity, to name a few reasons. Spatially variable materials can be human-made such as concrete, foams, gels, and composites or natural such as plant and animal tissues, wood, soils, granular media, and Earth's crust at larger length scale [1]. Understanding the behavior of heterogeneous materials has significant relevance in many areas, such as Engineering, Biology, Geophysics, Materials Science, and Physics. One can describe heterogeneous materials by quantifying spatial distribution of their mechanical properties at the micro or macro scale, depending on the purpose of the analysis.

Email address: s.szyniszewski@gmail.com (S. Szyniszewski)

Mechanical properties are usually obtained from uniaxial compression and tension, bending, torsion, or similar laboratory experiments. Conventionally, in all these cases, materials are assumed homogeneous throughout a sample. Whereas high-resolution of the optical or x-ray strain measurements help to identify defects or cracks, the extraordinarily granular information (e.g. $1000 \times 1000 = 10^6$ pixels with six components of the strain tensor per pixel) is usually averaged and a straight line is fitted into stress-strain data points, [2] in order to estimate Young's modulus. Nano-indentation tests are also leading to important advances in material heterogeneity analysis, most studies are focused on developing the testing methodology itself [3–6], while others are researching how considerable scatter inherent in the indentation load-displacement traces can be addressed in inverse analysis [7]. Note that fluctuations of displacements and strains across the sample reflect the variation of material properties throughout the field.

“Full-field measurement techniques”, developed since the 1980s, enable measurement of physical quantities at the surface or across the volume of a specimen. Such tools can determine displacement, strain, and temperature variations [8]. The digital image correlation (DIC) technique is one example for full-field measurements, and is widely used nowadays. This technique compares digital photographs of a specimen under loading at different stages of deformation. A software, underpinned by statistical computations, tracks movements of blocks of pixels in order to build up full-field deformation fields and resulting strain maps [9]. A 3D-extension of the 2D digital image correlation was presented by Bay et al. [10], called “digital volume correlation” (DVC), where the “digital volume” is generated by a 3D imaging method such as microtomography or micro-computed tomography (μ CT) [11]. The method was first applied to the measurement of strains in bone tissue. The technique is “the extension of area pixels subsets into volume voxel subsets”, and in the case of proper material texture, the subsets can be tracked using correlation procedures [12]. Thus, full-field measurement techniques can be specifically used to measure heterogeneous strain fields. An in-depth description of such methods is beyond of the scope of the present study, however, one can note that DVC, and, DIC techniques can be enhanced given the model developed by the authors.

When material’s properties are known, finding stress and strain distributions for a given geometry, boundary conditions, loading, and a particular material is trivially calculated. Conversely, finding stress and material property fields from given strain information and global loading is an example of an inverse problem. The stress field is the missing link between the full-field strain measurement and the spatial distribution of material properties. The finite element model updating (FEMU) technique [13–17], the constitutive equation gap method (CEGM) [18, 19], the equilibrium gap method (EGM) [20, 21], the reciprocity gap method (RGM) [22, 23] and Virtual Field Method (VFM) [24, 25] are some examples that have been proposed to solve the inverse problem for identification of parameters governing constituting equations. Grediac et al. [26] compares these methods and states that “the most popular method is the finite element model updating technique, which involves constructing a finite element model of the mechanical test, collecting displacement or strain components at some nodes and building up a cost function with the difference between numerical and experimental displacements at these nodes.” In this method, the solution is provided by

minimizing the cost function with respect to unknown constitutive parameters. Due to its flexibility, the FEMU technique does not specifically require full-field measurements [26]. The VFM, on the other hand, requires the availability of full-field data, as it solves a complete inverse problem by reformulating it [27]. The method takes into account the equilibrium of deformable solids, in the weak form by the principle of the virtual work and is used to identify linear elastic constitutive parameters from experimental displacement fields; VFM is fully detailed in [8].

Here, a simple, yet accurate technique, is proposed to identify material properties of a given specimen. The present approach requires the availability of full-field data, which is employed to FEMU technique using an analytical constitutive relationship to determine spatial distribution of Young's modulus and Poisson's ratio in the consecutive iterations. The proposed method uses an analytical expression to update elastic parameters at an element level (no global cost function is required). The method presented herein requires experimental data such as the magnitude of the applied loading, boundary conditions, and strain field, which can be obtained by full-field measurement techniques such as DIC, or a 3D extensions such as DVC. In order to demonstrate the proposed approach, laboratory tests and full-field strain measurements are mimicked by virtual experiments such that the material properties are known exactly for benchmarking of the proposed approach. The material properties are modeled as stationary random fields employing a set of correlation functions. The virtual benchmarking technique is used to test the proposed algorithm on 2D plates and 3D components.

2. Physics-based approach

The proposed algorithm aims at the determination of spatial distribution of Young's modulus, E , and Poisson ratio, ν , i.e. at the computation of elastic properties in *all* points. It requires the knowledge of the strain field, sample geometry, global loading, and boundary conditions. The approach employs a novel updating algorithm that combines analytical and numerical methods in an iterative process. The method uses physics-based, constitutive relationship to update the finite element model, and is not based on the minimization of the error cost function, which is typical for generic, parameter fitting methods.

As described by [8], problems concerning deformable solids involve displacement vector, \mathbf{u} and two second-rank tensors: strain tensor, $\boldsymbol{\varepsilon}$ and stress tensor, $\boldsymbol{\sigma}$. The equilibrium of any point of a solid's interior and its boundary, is given by:

$$\begin{cases} \operatorname{div}(\boldsymbol{\sigma}) + \mathbf{b} = 0 \\ \boldsymbol{\sigma} \cdot \mathbf{n} = \boldsymbol{\sigma}_n \end{cases} \quad (1)$$

where,

\mathbf{b} is the body force vector;

$\boldsymbol{\sigma} \cdot \mathbf{n}$ is the normal flux on the boundary;

\mathbf{n} is the normal vector on the boundary.

For linear, elastic isotropic material behavior, the stress-strain equation can be written as:

$$\boldsymbol{\sigma} = \mathbf{C}\boldsymbol{\varepsilon} \quad (2)$$

where \mathbf{C} is the stiffness tensor, which can be written as a matrix function of the Young's modulus, E and Poisson's ratio, ν parameters.

Our goal is to find $E(\mathbf{x})$, and $\nu(\mathbf{x})$ as a function of position within the solid, \mathbf{x} taking advantage of the physical relationships between the stress, $\boldsymbol{\sigma}(\mathbf{x})$ and strain, $\boldsymbol{\varepsilon}(\mathbf{x})$. Our approach assumes local and global isotropy of the material. The details of the proposed method are presented in this section.

2.1. Updating algorithm

This section explains the physics-based updating principle in 1-D context for simplicity, before the method is generalized to two- and three-dimensions in the latter parts of the article. Our algorithm is based on the insight that regions with lower strain represent stiffer material, while higher strains correspond to softer patches; however, strains are redistributed across the volume such that deformations of soft patches are limited by their stiffer neighbors, and stiffer spots experience larger strains by partially carrying the loading of their softer neighbors. Thus, one cannot use constitutive relationships to compute material properties without solving the equilibrium equations; however, one might use the constitutive relationships to *update* material constants.

Let us consider a situation, where principal strain is known from the experiment, ε_1^* , where * indicates measured quantity, which is assumed to be correct and the true value. We are also able to estimate principal stress, σ_1^i and principal strain, ε_1^i in that location using a computational, finite element model. These estimates are initially not correct but improve from iteration i to $i+1$ and so on. Here, we propose to use the measured strain in conjunction with the estimated, simulated stress to update the finite element model as follows. Smaller measured strain $\varepsilon_1^* < \varepsilon_1^i$ indicates that the actual material is stiffer than the simulated one, i.e. $E^* > E^i$. Thus, we would like to update Young modulus in such a way that $E^{i+1} > E^i$ to stiffen the element. We can achieve that by using a constitutive relationship with the real strain, ε_1^* and simulated stress, σ_1^i to compute Young modulus at the next iteration, $i + 1$:

$$\left(E^{i+1} = \frac{\sigma_1^i}{\varepsilon_1^*} \right) > \left(E^i = \frac{\sigma_1^i}{\varepsilon_1^i} \right) \quad (3)$$

because

$$\varepsilon_1^* < \varepsilon_1^i \quad (4)$$

Conversely, if the measured strain, ε_1^* is larger than the simulated one, ε_1^i using the real strain with the simulated stress in the constitutive relationship 'softens' the material constant at the next iteration, $i + 1$:

$$\left(E^{i+1} = \frac{\sigma_1^i}{\varepsilon_1^*} \right) < \left(E^i = \frac{\sigma_1^i}{\varepsilon_1^i} \right) \quad (5)$$

because

$$\varepsilon_1^* > \varepsilon_1^i \quad (6)$$

Therefore, using measured strains, indicated with * against simulated stress at iteration i to update material constants in iteration $i+1$ softens or stiffens the material relatively to the magnitude of the difference between the measured and simulated strains. If both the simulated and measured strains are equal, the iterative algorithm has converged and the simulated material properties at the current iteration are the unique solution corresponding to the measured strain field *. One could also stop the updates if the last iteration produces a negligible, incremental change, for example, if:

$$\left| \frac{E^{i+1} - E^i}{E^i} \right| < 1\% \quad (7)$$

2.2. Generalization to three-dimensions

Elastic properties of three-dimensional bodies can be characterized with two elastic constants, such as Lame parameters, μ and λ , or any combination of two of the three engineering elastic constants such as Young modulus, E , shear modulus, G or Poisson ratio, ν . In order to ensure that ν does not exceed the allowable limits, the algorithm was implemented using the *coupled*, constitutive relationship in a matrix format directly. The use of *principal* strains and stresses assures that our updating algorithm is also independent of the frame of reference and applicable to non-trivial stress states:

$$\begin{bmatrix} \varepsilon_1^* \\ \varepsilon_2^* \\ \varepsilon_3^* \end{bmatrix} = \begin{bmatrix} \frac{1}{E^{i+1}} & \frac{-\nu^{i+1}}{E^{i+1}} & \frac{-\nu^{i+1}}{E^{i+1}} \\ \frac{-\nu^{i+1}}{E^{i+1}} & \frac{1}{E^{i+1}} & \frac{-\nu^{i+1}}{E^{i+1}} \\ \frac{-\nu^{i+1}}{E^{i+1}} & \frac{-\nu^{i+1}}{E^{i+1}} & \frac{1}{E^{i+1}} \end{bmatrix} \begin{bmatrix} \sigma_1^i \\ \sigma_2^i \\ \sigma_3^i \end{bmatrix} \quad (8)$$

Since two material constants are updated at each iteration, we need to arbitrarily select two equations such as the one for the maximum principal strain:

$$\varepsilon_1^* = \frac{1}{E^{i+1}} (\sigma_1^i - \nu^{i+1} \sigma_2^i - \nu^{i+1} \sigma_3^i) \quad (9)$$

and the minimum principal strain:

$$\varepsilon_3^* = \frac{1}{E^{i+1}} (-\nu^{i+1} \sigma_1^i - \nu^{i+1} \sigma_2^i + \sigma_3^i) \quad (10)$$

For thin plates, exhibiting a 2D stress state with $\sigma_2 = 0$, the system of equations for the next update of E^{i+1} and ν^{i+1} is:

$$\begin{cases} \nu^{i+1} = \frac{-\varepsilon_3^* \sigma_1^i + \varepsilon_1^* \sigma_3^i}{\varepsilon_1^* \sigma_1^i - \varepsilon_3^* \sigma_3^i} \\ E^{i+1} = \frac{\sigma_1^i - \nu^{i+1} \sigma_3^i}{\varepsilon_1^*} \end{cases} \quad (11)$$

2.3. Coupling with finite element model

Firstly, the strain field is obtained from the full-field measurement technique (FFMT). The data needs to be saved into text, csv or sql file for convenient access by a script iteratively computing material properties across the sample. Material properties were updated using Matlab implementation of the algorithm. The finite element model of the tested sample (“digital twin”) is also created such that its mesh matches the resolution of the full-field strain measurement. The aim is to achieve a one-to-one correspondence between the discrete grid of the measured strains and simulated stresses at element centroids as well as material properties. A finite element model is subjected to the known global load, and it generates strain and stress fields as output; however, only the stress tensor data is needed in our iterative approach. A ’digital twin’ computational simulation involves:

- choosing the analysis type: 2D or 3D,
- creation of a model with dimensions corresponding to the experimental sample,
- discretization of the domain into elements matching the grid of the measured strains,
- application of boundary conditions,
- parametrization of material properties in all elements: $E(\mathbf{x}_k)$ and $\nu(\mathbf{x}_k)$, where $k =$ element number.

The flowchart of the proposed *Physics-based* Finite Element Updating method (*PB-FEUM*) is described in Figure 1. We initialize the stress state using average material constants obtained using conventional techniques. Average stress (applied force divided by the specimen area) and average strain from the full field measurement or strain gauges can be used to estimate mean material properties, to providing starting values for the algorithm. Next, the initial stress state and the measured strains allow for computation of updated material constants in all elements. Subsequently, the finite element model is updated with the new material constants to enable calculations of stresses in the next step. It is important to note that while material properties and stresses are updated at each iteration, the strains are held *constant* for updating material parameters because these come from measurements and are considered ’true’ values. The finite element analysis is updated with the new material properties $E^{i+1}(\mathbf{x}_k)$ and $\nu^{i+1}(\mathbf{x}_k)$ across all elements.

The flowchart stops by reaching the maximum, allowed number of iterations. Although, strain convergence can be also checked, it has not been used as a criterion to stop the iterations. The updates continue until incremental change is deemed negligible compared to the previous iteration. The specific selection of the termination criterion depends on the trade off between the computational time and the desired level of accuracy. One possible criterion for stopping the iteration is when the norm of the relative change between two consecutive iterations is less than 1%.

3. Methods

To test the proposed algorithm, we simulated compressive experiments of solid and plate samples with random fields of elastic material properties. The advantage of such 'virtual experiments' is that all material properties are known. It enables comparison of the property fields computed by the proposed algorithm (based on the supplied strain field information) against the original material data in the virtual experiment simulation. We have considered stochastic fields with correlation scales ranging from element size to the sample size as well as various levels of cross-correlations between the material constants. This section explains the generation of the suite of samples with stochastic material distributions for the benchmarking of our proposed algorithm.

A stationary random field characterized by its marginal distribution and second moment properties is used to model the variability of solid's material properties in this study [1]. The covariance measurement is based on the separation distance between each pair of elements in the numerical analysis, which is defined by a covariance function. The Squared Exponential covariance function is chosen for this model, which is often used to describe autocovariance of soil properties [28]. The covariance function, also known as kernel is from [1] as follows:

$$k = \exp\left(-\frac{r^2}{\gamma^2}\right) \quad (12)$$

The selected kernel allows the user to control the distance for which the correlation between the elastic parameters of two elements is negligible. The control is set by the constant γ , which is associated with the spatial frequency in the field [29]. Therefore, the scale γ defines the spatial rate of material variations. The correlation function also depends on the distance between the elements' centroids, defined by r . A matrix R_{mm} holds all distances between each pair of elements ($r = \sqrt{(\mathbf{x}_i - \mathbf{x}_j)^2}$), calculated using coordinates of elements centroids $\mathbf{x}_{<k>}(x, y, z)$:

$$\mathbf{R}(\mathbf{x}) = \begin{pmatrix} \sqrt{(\mathbf{x}_1 - \mathbf{x}_1)^2} & \sqrt{(\mathbf{x}_1 - \mathbf{x}_2)^2} & \cdots & \sqrt{(\mathbf{x}_1 - \mathbf{x}_m)^2} \\ \sqrt{(\mathbf{x}_2 - \mathbf{x}_1)^2} & \sqrt{(\mathbf{x}_2 - \mathbf{x}_2)^2} & \cdots & \sqrt{(\mathbf{x}_2 - \mathbf{x}_m)^2} \\ \vdots & \vdots & \ddots & \vdots \\ \sqrt{(\mathbf{x}_m - \mathbf{x}_1)^2} & \sqrt{(\mathbf{x}_m - \mathbf{x}_2)^2} & \cdots & \sqrt{(\mathbf{x}_m - \mathbf{x}_m)^2} \end{pmatrix} \quad (13)$$

The correlation matrix K_{mm} , holds the correlation between all pairs of elements k_{ij} using equation (12), which is a function of the matrix \mathbf{R} and the scale γ :

$$\mathbf{K}(\gamma, \mathbf{R}) = \begin{pmatrix} k_{11} & k_{12} & \cdots & k_{1m} \\ k_{21} & k_{22} & \cdots & k_{2m} \\ \cdots & \cdots & \ddots & \vdots \\ k_{m1} & k_{m1} & \cdots & k_{mm} \end{pmatrix} \quad (14)$$

Matrix \mathbf{K} in equation (14) is then decomposed by the singular value decomposition method, such that:

$$\mathbf{K} = \mathbf{U} \mathbf{S} \mathbf{V}^T \quad (15)$$

The product of the left singular vector \mathbf{U} and the square root of the diagonal matrix \mathbf{S} , multiplies a Gaussian random and uncorrelated variable $\phi_{m \times 1}$, generating a random but correlated distribution $\Phi_{m \times 1}$:

$$\Phi = \mathbf{U} \sqrt{\mathbf{S}} \phi \quad (16)$$

The random but spatially correlated variable vector with zero mean and unit standard deviation is then scaled by multiplying Φ by a standard deviation std and summed to an average variable value μ :

$$\mathbf{E}(\mathbf{x}_k) = \Phi_k^E std_E + \mu_E \{\mathbf{1}\} \quad (17)$$

and,

$$\boldsymbol{\nu}(\mathbf{x}_k) = \Phi_k^\nu std_\nu + \mu_\nu \{\mathbf{1}\} \quad (18)$$

Here, Young modulus and Poisson ratio are two *independent* realizations (indicated with superscripts E and ν) of random variables with spatial correlation (characterizing the spatial rate of change). In the analysis presented in this work, the kernel's scale of fluctuation varies from element's size of the mesh (high variability) to sample's length (smooth field). Coefficients of variation of Young's modulus (Δ_E) and Poisson's ratio (Δ_ν) were also defined in order to account for the variability of the constants. Note that there are other methods available to create random fields, which do not alter the authors' conclusions and proposed methodology.

3.1. Stochastic field for two or more correlated variables

The elastic material properties may also be *cross-correlated* over the field. The magnitude of the cross-correlation (β), varying from 0.0 to 1.0, defines how similar the magnitude of Young's modulus and Poisson's ratio are in each element. In case of cross-correlation between variables, the correlation function for matrices $\mathbf{K}_{E\nu}$ and $\mathbf{K}_{\nu E}$ are stated as:

$$k = \beta \cdot \exp\left(-\frac{r^2}{\gamma^2}\right) \quad (19)$$

and the global correlation matrix consists of four matrices, as follows:

$$\mathbf{K}_c = \begin{pmatrix} \mathbf{K}_{EE} & \mathbf{K}_{E\nu} \\ \mathbf{K}_{\nu E} & \mathbf{K}_{\nu\nu} \end{pmatrix} \quad (20)$$

where,

\mathbf{K}_{EE} is the correlation matrix of Young's modulus.

$\mathbf{K}_{\nu\nu}$ is the correlation matrix of Poisson's ratio.

$\mathbf{K}_{E\nu} = \mathbf{K}_{\nu E}^T$ are the correlation matrices between Young's modulus and Poisson's ratio, calculated using equation (19).

3.2. Benchmark features

The basic values of each parameter considered in this study are presented in Table 1. The mean values of Young's modulus and Poisson's ratio considered in the analyzes are 29269 MPa and 0.203, respectively. Figure 2 illustrates examples of two-dimensional random fields for a 2D plate with 1m x 1m, and 50 x 50 elements. The surfaces vary depending on the cross-correlation between variables (β), coefficient of variation (Δ) and scale of fluctuation (γ), which is sometimes also called correlation length. One can note how changing each parameter affects the surface characteristics. When the material properties are perfectly correlated, the variables' surfaces are the same. High coefficient of variation generates peaks of low and high values. The difference in the field fluctuation scale illustrates how variable or smooth a correlated random field may be by setting the scale of fluctuation, γ parameter.

Table 1: Random field parameters

Property	Parameter	Value
Correlation between E and ν	β	0.5
Coefficient of Variation	Δ	0.1
Scale of fluctuation	γ	0.25

In order to represent a wide range of laboratory experiments (cylinder, cube or a more specialized shape) three dimensional cases are also considered. The proposed PB-FEUM algorithm for the computation of material properties is tested using a range of three-dimensional blocks with various distributions of material properties under uniform compressive loading. Such cases correspond to typical compressive experiments. Three-dimensional random fields for a cube of size 1 meter employed for benchmarking are presented in Figure 3.

In summary, we run a number of benchmark simulations, called Virtual Experiments (VE) first. Each analysis employs a stochastic field of material properties and is used as a benchmark for the proposed iterative algorithm, PB-FEUM, which uses only the FFMT strain field from VE. While using virtual experiments allows us to assess the accuracy of the algorithm, there is no experimental uncertainty nor noise in this analysis. Note that Section 4.3 addresses the topic of experimental noise.

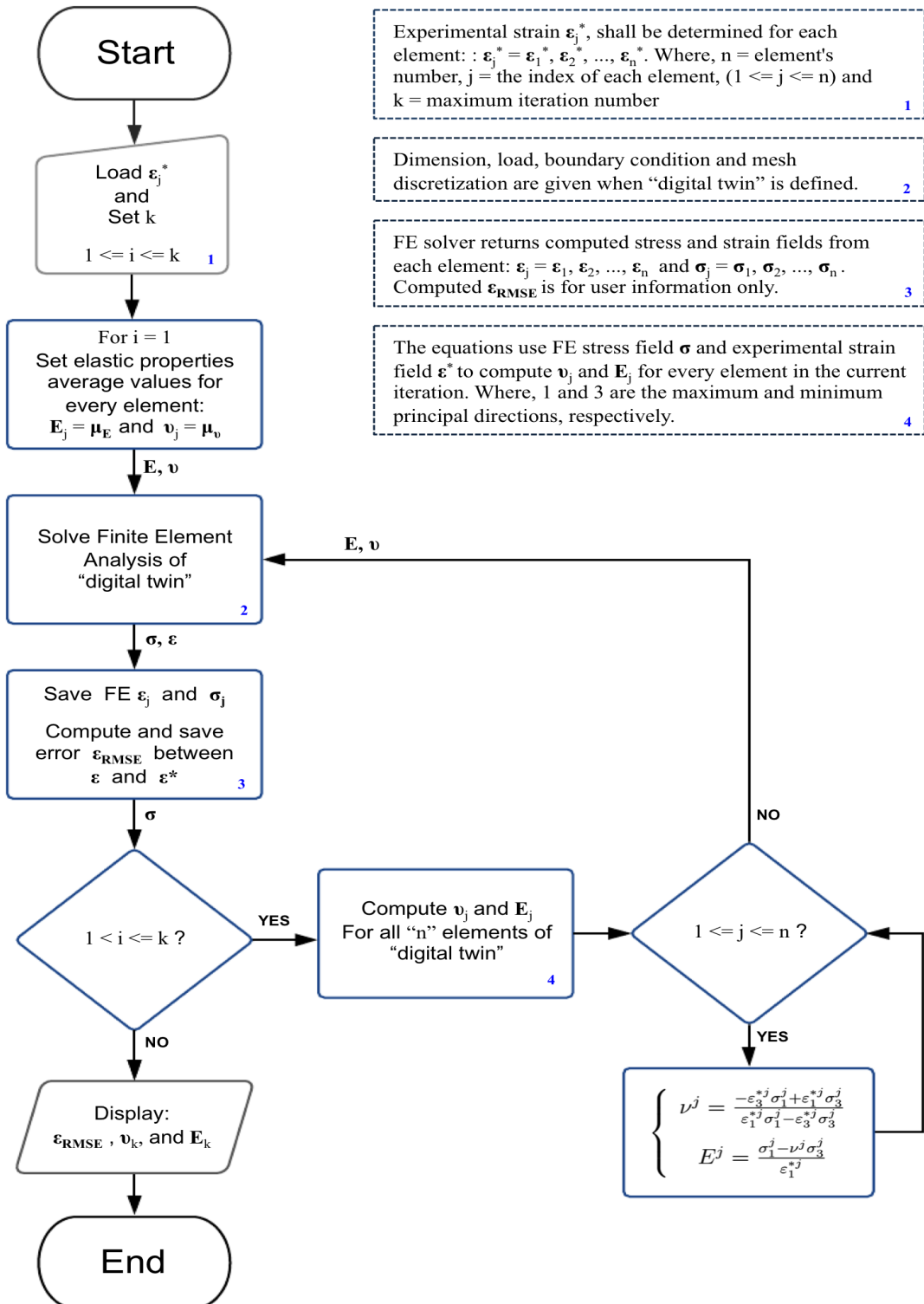


Figure 1: Physics-based Finite Element Updating method (PB-FEUM) flowchart.

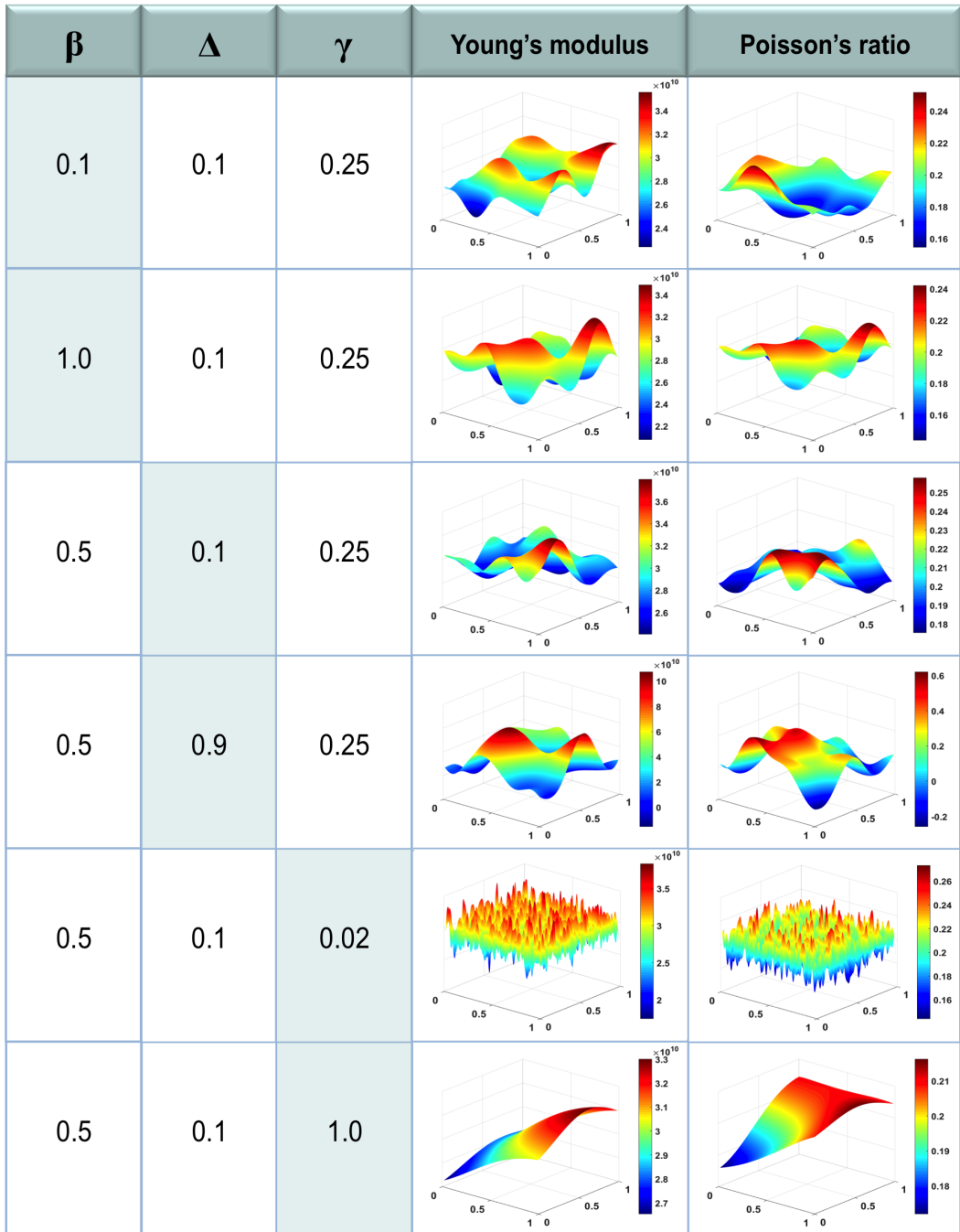


Figure 2: 2D Random Fields based on β (cross-correlation), Δ (coefficient of variation), and γ (scale of fluctuation).

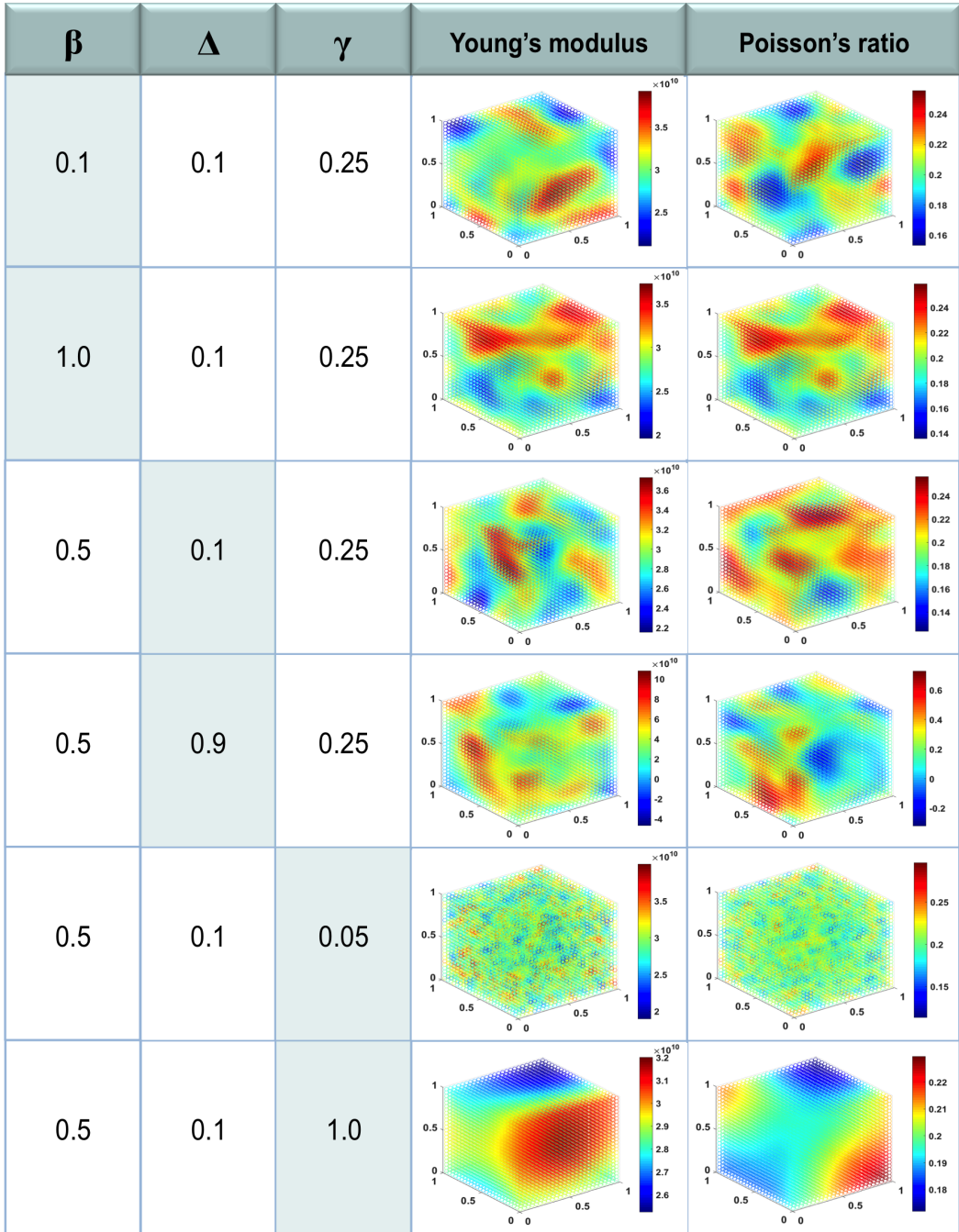


Figure 3: 3D Random Fields based on β (cross-correlation), Δ (coefficient of variation), and γ (scale of fluctuation).

In order to quantify the accuracy of the iterative algorithm, we used the Root Mean Square Error (RMSE), which is the standard deviation of the residuals between the VE material properties (constant through the process) and material parameters computed at each iteration by PB-FEUM:

$$RMSE_v = \sqrt{\sum_{i=1}^m \frac{(v_i - v_{VE})^2}{m}} \quad (21)$$

Where, m is the number of finite elements, and v refers to a variable (Young's modulus or Poisson's ratio) from the iterative solution, and v_{VE} represents the Virtual Experiment variables.

For convenience, the $RMSE_v$ is normalized by the mean values of the VE elastic field. Thus, the normalized value represents the mean residual in the property estimation. Table 2 summarizes all the cases analyzed in the next section (including 2D and 3D models).

Table 2: 2D and 3D scenarios analyzed

Model	Dimension (m)	Element's size (m)	Tested parameters
2D	$1.0 \times 1.0 \times 0.02$	0.1 or 0.02	γ, β, Δ
3D	$1.0 \times 1.0 \times 1.0$	0.04 or 0.05	γ

4. Results and discussion

4.1. 2D cases under in-plane loading

A VE model, created in ABAQUS, represents a compression laboratory test of a 2D flat specimen numerically. The plate has the size of 1 m x 1 m x 0.02 m and is discretized with 100 elements (a square mesh with 10 x 10 elements) and 2500 elements (50 x 50 elements) as shown in Figure 4. The spatially correlated fields for Young's modulus and Poisson's ratio, with mean values shown in Table 1, and normal distribution functions are used for material modeling in both cases. A uniform pressure of 19.5 MPa is applied to the top of the plate and plane stress formulation is used. The plate is supported along the bottom edge by constraining in-plane displacements in the direction of loading (y-axis) and one node in the base of the plate in the transverse and out-of-plane directions (x- and z-axis) for stability.

Once the strain data is obtained from VE (or in the laboratory test by FFMT) and the mean values of the material properties are known, the iterative process may proceed. Figures 5 and 6 present the convergence of elastic parameters after 15 iterations, for a range of random material fields (E, ν) with γ of 0.1 and 1.0. Value of $\gamma = 0.1$ represents the most variable field, while $\gamma = 1.0$ gives the smoothest field. Both cases have the same, partial cross-correlation $\beta = 0.5$ between material variables and normalized coefficient of variation $\Delta = 0.1$. The random field generated for the VE is compared with the last iteration of the proposed iterative algorithm, in order to check the accuracy and efficacy

of the proposed method. The last row of the comparative figures gives reference fields of Young's modulus and Poisson's ratio employed in the virtual experiment. These can be compared with the gradual evolution of the material property maps as they update from iteration to iteration. The first row shows the starting iteration using constant fields based on the average values of Young's modulus and Poisson's ratio. We used material properties corresponding to a limestone type material, with $E_{avg} = 29.27 \text{ GPa}$ and $\nu_{avg} = 0.203$. Color scales for the plots are constant for each case, with the minimum and maximum computed from the last iteration of the iterative process. Thus, the colors of the starting, constant value plots differ, but they correspond to the same average starting values. The iterative process reaches satisfactory results when compared to VE for all considered fluctuation scales. The proposed approach is also suitable for highly heterogeneous fields. The solution from the iterative method for a mesh of 2500 elements with short fluctuation scale of $\gamma = 0.02$, $\Delta = 0.1$ and $\beta = 0.5$ showed excellent agreement with the distributions of the material properties in the benchmark models (Figure 7).

One can track the convergence of the algorithm by comparing simulated strains (updated at each iteration) to experimental strains (measured, reference values). Once simulated material properties match the actual specimen, the computed strains also conform to the measured values. The evolution of the Root Mean Square Error (RMSE) of the axial, transverse and shear strains is shown in Figure 8. Shear strain field under axial compression in the original cartesian frame of references has values approaching zero. Thus, shear strain convergence (in the original frame of reference) is the most affected by numerical accuracy, round off errors and exhibits the slowest convergence rate. Nevertheless, the final convergence of the shear strains indicates that the same state of equilibrium is reached in the model as in the tested specimen. Shear strains result from the load redistribution between stiffer and softer material regions across the sample. By investigating the RMSE of the strains, the end-user has an option of assessing the convergence of the algorithm and stop the iterations once the desired accuracy is reached.

In order to determine the efficacy of the proposed algorithm in the latter sections, we use RMSE of the *material constants*, namely Young's modulus and Poisson's ratio, against the values employed in the virtual experiments because it is the explicit metric of the algorithm accuracy. The RMSE for the cases shown in Figures 5, 6, 7 are presented in Figure 9. The error between the calculated values of E and ν and the VE reference values of the same variables exponentially decreases as iterations progress. As expected, low values of the spatial fluctuation length γ present larger error in the last iteration when compared to smoother fields; however, the three cases still exhibited RMSE lower than 4% for both elastic parameters in the last considered iteration.

A sensitivity analysis of the proposed algorithm to variations of the three random fields parameters: γ , Δ , and β is also investigated. The RMSE of the last iteration in each process, for values of fluctuation scale, γ varying from 0.02 to 1.0; coefficient of variation, Δ changing from 0.01 and 0.5 and cross-correlation between the variables, β in a range between 0.01 and 1.0 are shown in Figure 10. Two random simulations for each case are presented. We vary only one stochastic parameter at the time, while the others are kept constant at the values shown in Table 1.

The obtained results in Figure 10 indicate that high values of spatial correlation scale, γ present lower error for both material variables because the field becomes smoother. On the other hand, high values of coefficient of variation, Δ increase the error for both variables, which is sensible because higher coefficient of variation increases the level of dispersion around the mean values. The cross-correlation, β , however, shows that high or low correlation between the material variables does not influence the solution's convergence. In all considered cases the RMSE is lower than 10%, and a satisfactory solution is reached after a dozen of iterations.

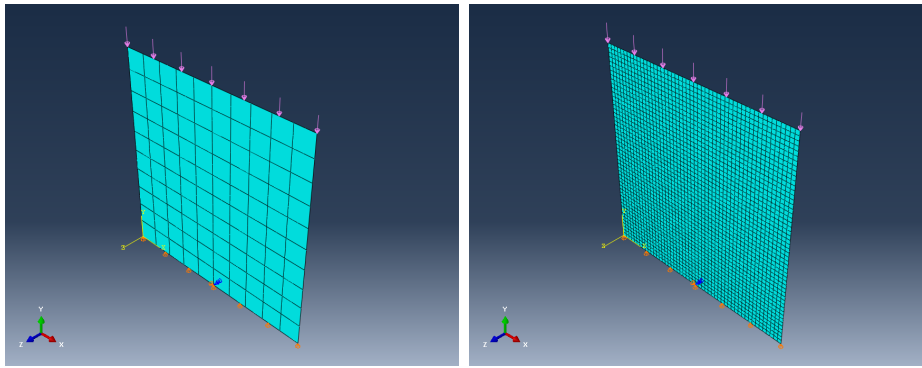


Figure 4: Virtual Experiments. 2D plates discretized with 100 (left) and 2500 elements (right).

4.2. 3D cases under uniform loading

Following 2D geometries, the proposed algorithm was evaluated for 3D cases. VE model was created in Abaqus software for benchmarking of our approach. A cube of 1m x 1m x 1m size is discretized with 8000 elements (a cubic mesh of 20 x 20 x 20 elements). The spatially correlated fields for Young's modulus and Poisson's ratio have values shown in Table 1. The cube is constrained at the bottom face in the out-of-plane direction and at two nodes in the base against movements in the other two directions (x- and z-axis) to restrain all rigid translations and rotations. A uniform pressure of 19.5 MPa is applied on top of the specimen.

The strains throughout the field are considered as known quantity from a laboratory test using a FFMT. In order to enable benchmarking of PB-FEUM algorithm, the strain data is obtained from the VE simulation for all elements, and it is supplied as input to the iterative process. The resulting fields of Young's modulus and Poisson's ratio after 15 iterations and their convergence are shown in Figures 11 and 12, and Figure 13. These cases consider two fluctuation scales, γ of 0.5 and 0.05. The employed stochastic fields have cross-correlation between Young modulus and Poisson ratio of $\beta = 0.5$ and coefficient of variation $\delta = 0.1$. The 3D cases, similarly to 2D benchmarks, demonstrate excellent convergence. The case with longer fluctuation scale, $\gamma = 0.5$ converges faster than the highly discontinuous case with $\gamma = 0.05$. That trend is consistent with the observations of 2D cases discussed earlier. The proposed iterative algorithm estimated material constants with the mean normalized

error below 5% after as little as five iterations. However, the convergence rates vary from sample to sample, and can be different between random realizations of the same stochastic field (with fixed β , γ and Δ). This observation is consistent with a scatter of points in the γ sensitivity plots for 2D cases shown in Figure 10.

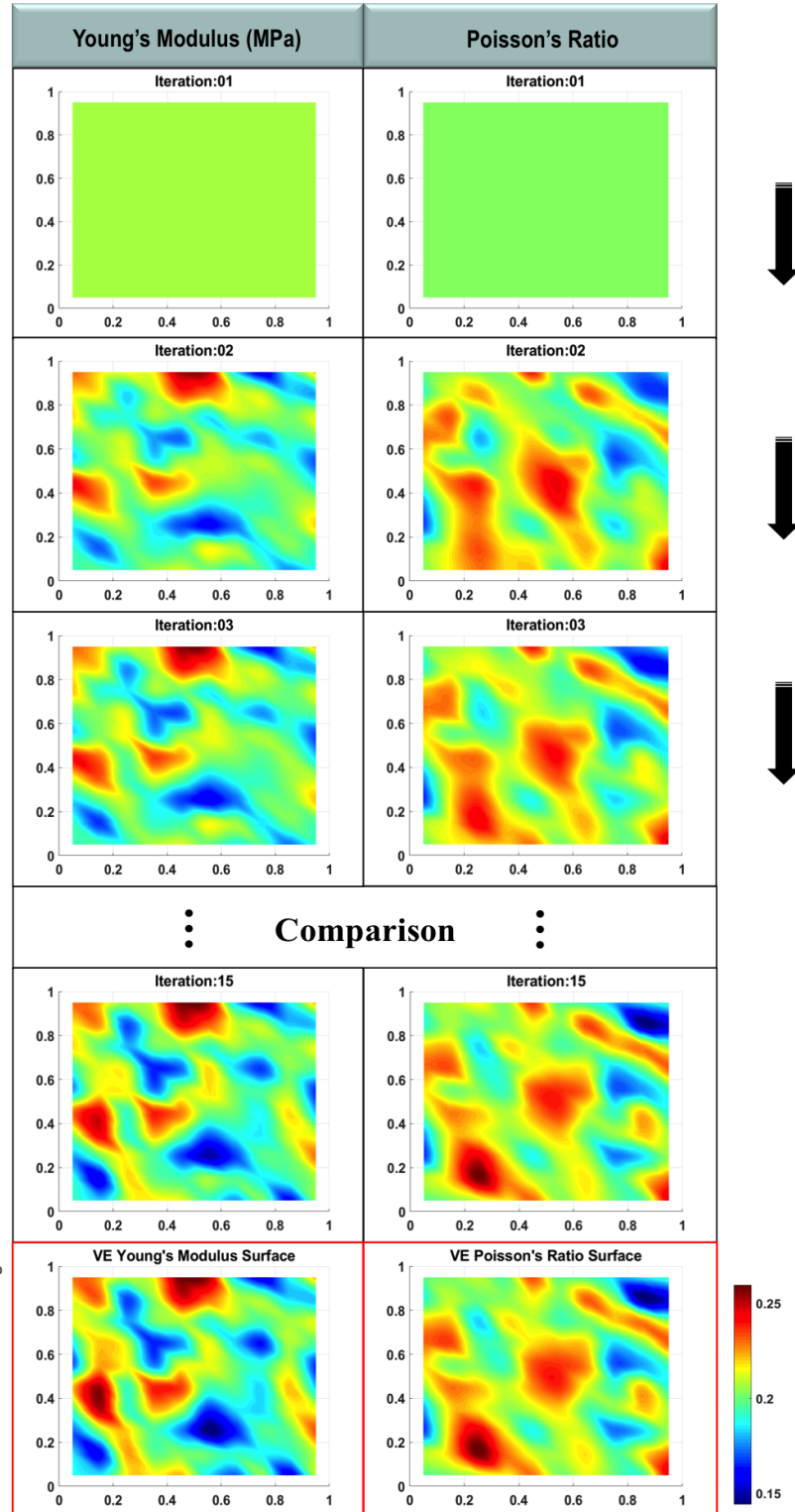


Figure 5: 2D iterative method for a mesh with 100 elements and $\gamma = 0.1$.

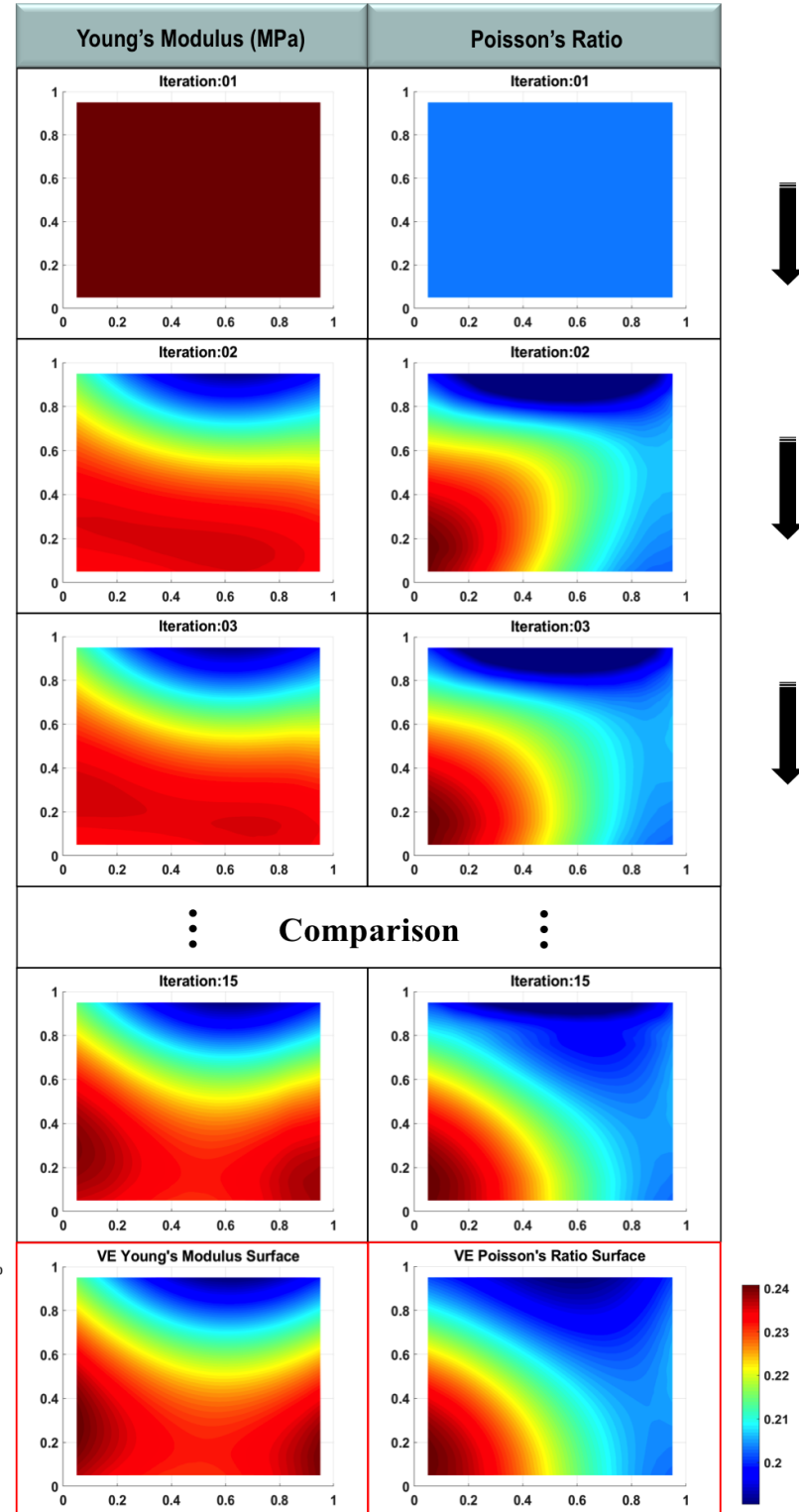


Figure 6: 2D iterative method for a mesh with 100 elements and $\gamma = 1.0$.

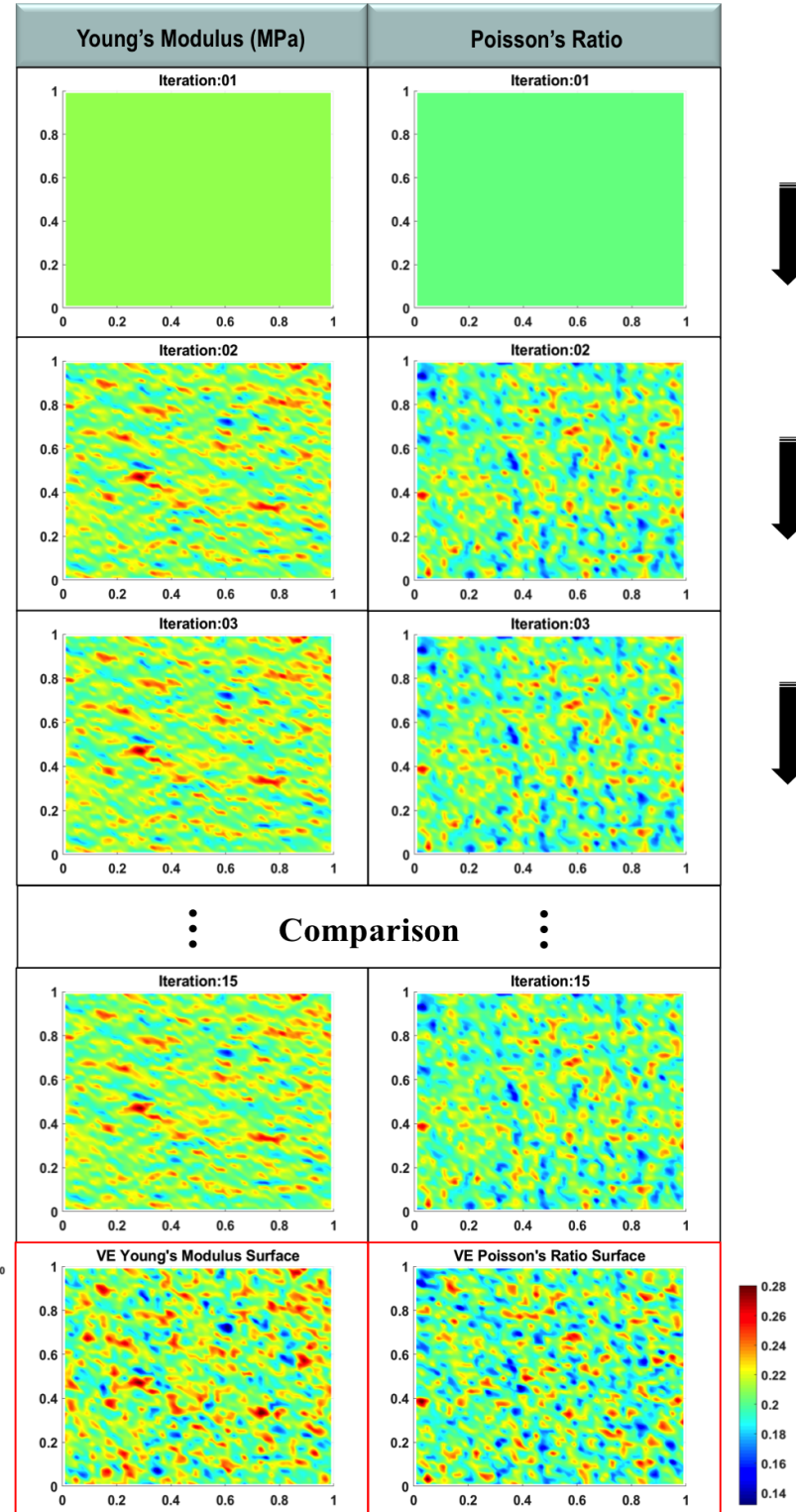


Figure 7: 2D iterative method for a mesh with 2500 elements and $\gamma = 0.02$.

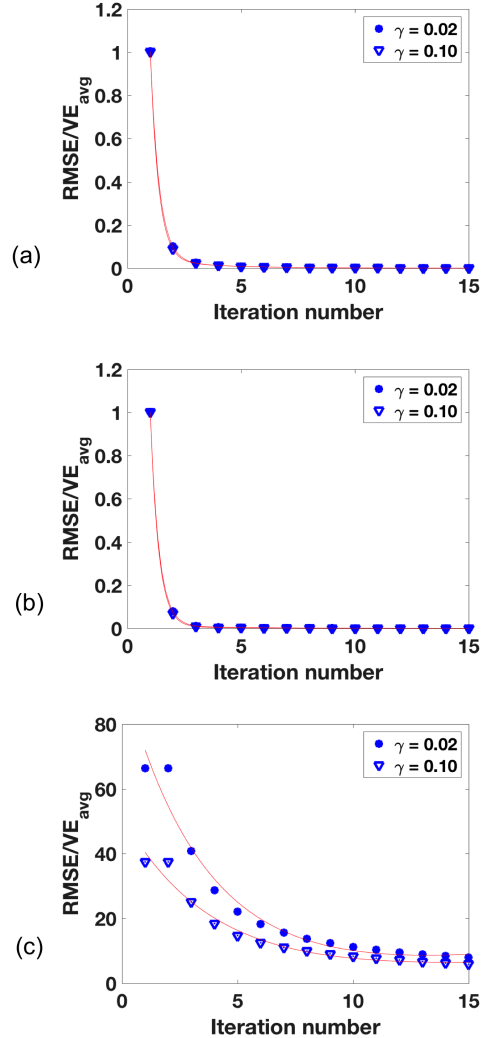


Figure 8: Normalized RMSE of the *strains* in (a) transverse (x-direction), (b) axial (y-direction), (c) shear strain, in each iteration for random 2D cases with $\gamma = 0.02$ and $\gamma = 0.1$.

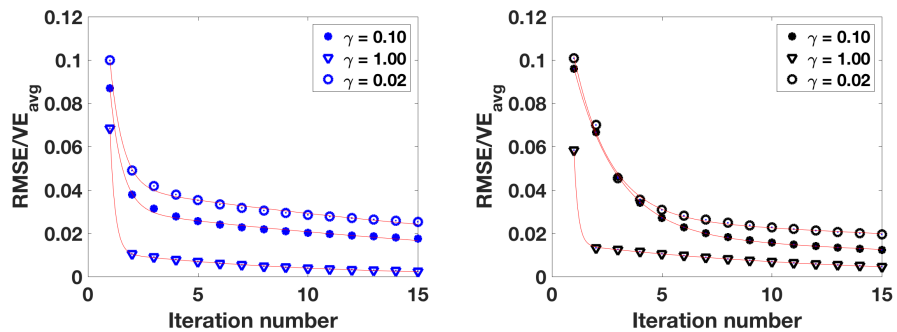


Figure 9: Normalized RMSE of E (left) and ν (right) in each iteration for the 2D cases.

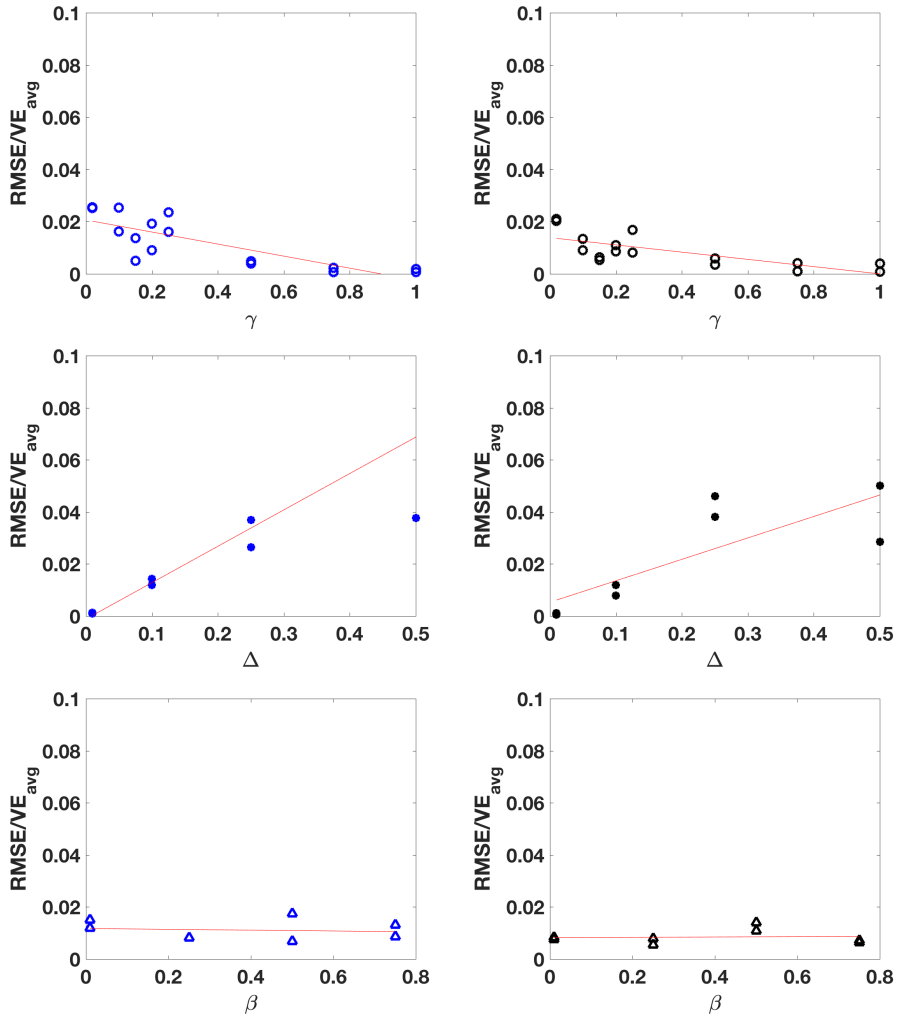


Figure 10: Normalized RMSE of E (left) and ν (right), when spatial correlation scale, γ , coefficient of variation, Δ , and cross-correlation, β parameters are varied.

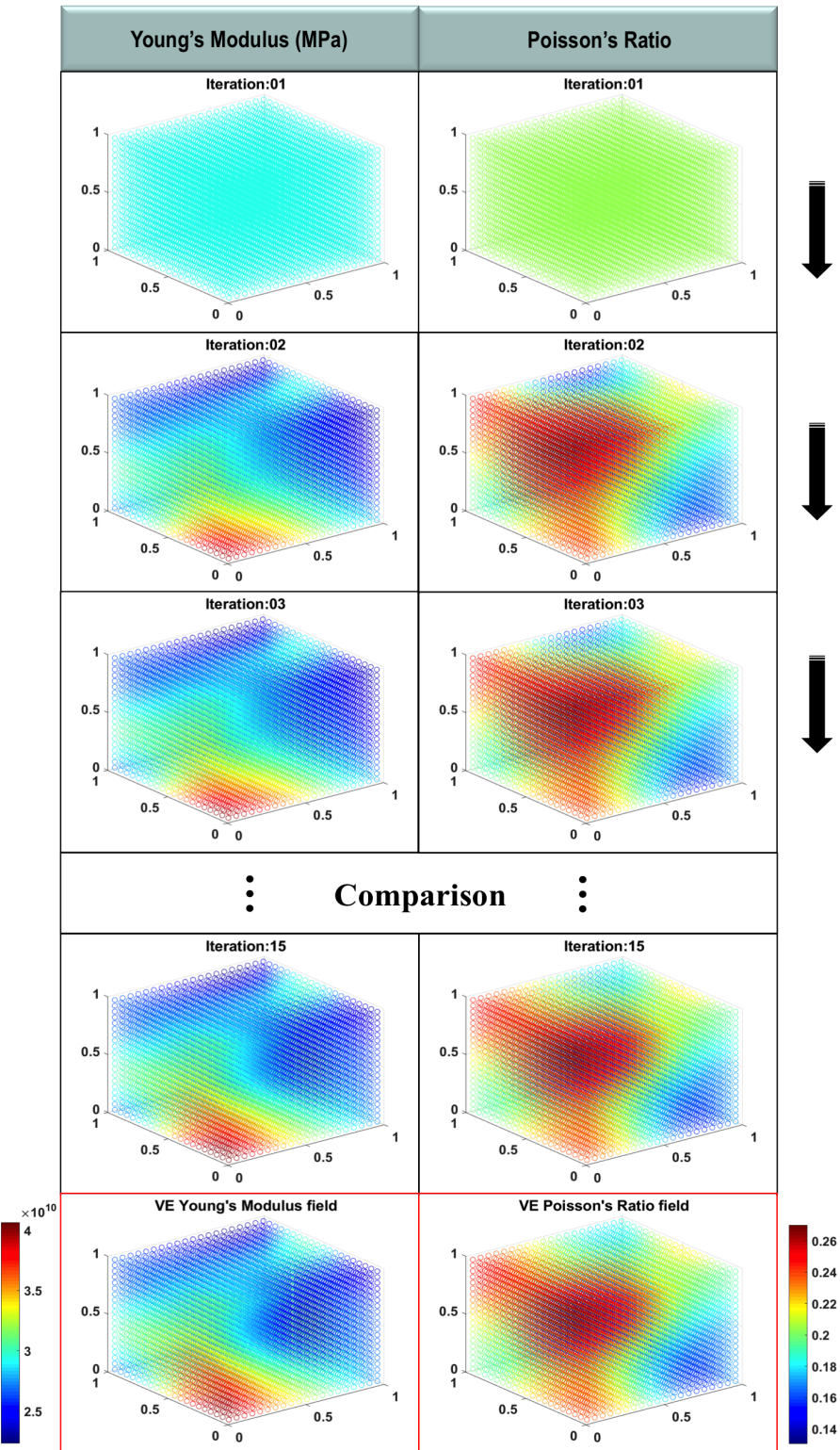


Figure 11: Comparison of material properties computed using 3D iterative method against VE benchmark data for a mesh with 8000 elements and $\gamma = 0.50$.

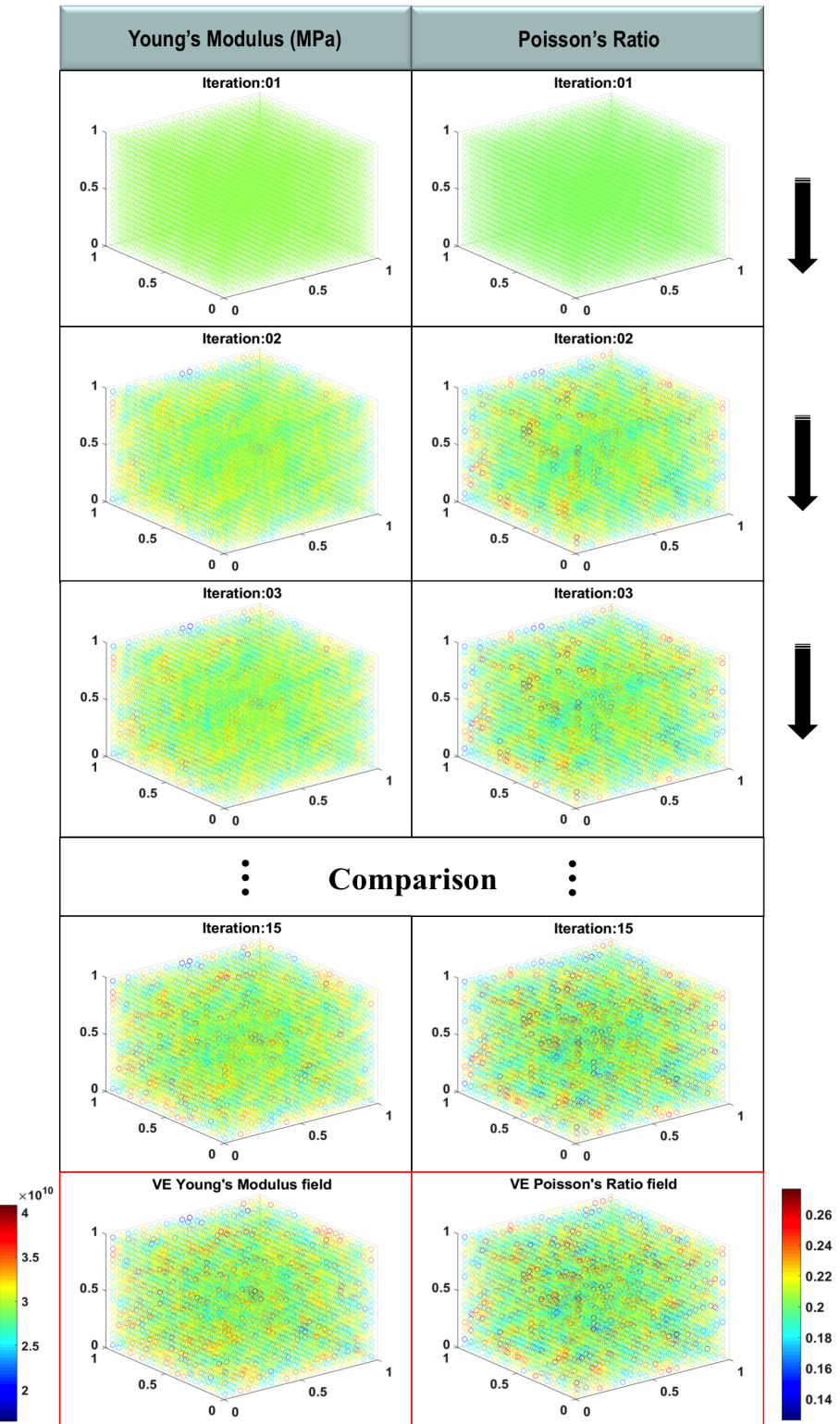


Figure 12: Comparison of material properties computed using 3D iterative method against VE benchmark data for a mesh with 8000 elements and $\gamma = 0.05$.

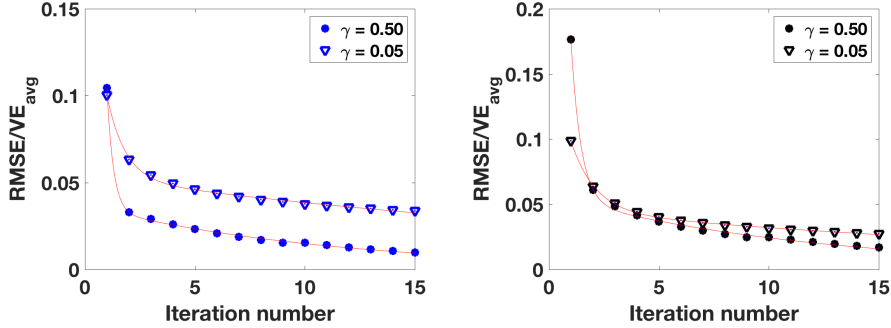


Figure 13: Normalized RMSE of E (left) and ν (right) in each iteration for the 3D cases.

4.3. Analysis of imaging noise

The measured strains are not perfect, and are affected by the measurement inaccuracies. Lava et al. [30] and Ross et al. [31] used numerical noise to perturb input fields to assess the robustness of their parameter identification methods. We employed a similar approach but also studied the nature of the noise and worked on the estimation of measurement noise amplitude as discussed below.

4.3.1. Assessment of the experimental, measurement noise

Our proposed measurement technique for 2D components, namely digital image correlation (DIC), will inherently produce measurement noise due to limitations of imaging. To assess the magnitude of the measurement error, we have estimated imaging error based on fluctuations in image greyscale values whilst a sample component was unloaded.

Two images (Figures 14a and 14b) were captured 1 second apart, with no component loading conducted. We compared the difference between each image, for every pixel position (Figure 14c), to measure how the two images differ. The images had size of 1344 x 1326 pixels. Virtual strain gauge (VSG) of 99 pixels was used, with the end locations of the VSG computed from two regions of 39 x 39 pixels.

We compared the greyscale intensity for a sample 39 x 39 pixel region using an in-built ImageJ function, and computed the standard deviation (σ) of pixel greyscale fluctuation between two images, without any component loading, as 1.248.

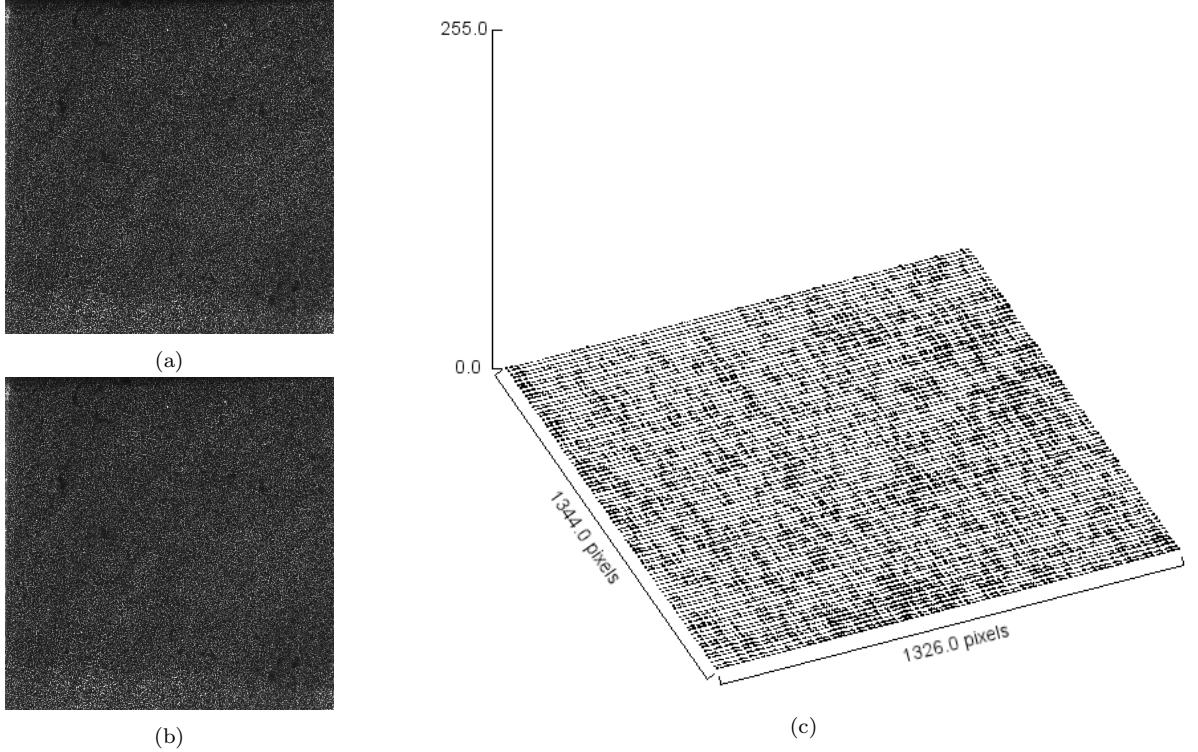


Figure 14: (left) Two images captured during experimentation without loading, which have been compared for greyscale intensities at each pixel. (right) Plot of the variation in intensities at each pixel location

Using the greyscale fluctuation, we calculated an estimate for our experimental worst case strain error. We conducted the benchmark assessment based on the error associated to digital imaging noise upon an algorithmic capability to locate a centroid of a given region, utilising the centroid tracking algorithm stated by Naidu and Raol [32] and given in Equation 22.

$$x_{n_c} = \frac{\sum_{k=1}^N x_{n_k} I_k}{\sum_{k=1}^N I_k} \quad (22)$$

This equation states that the center pixel along the x direction (x_{n_c}) of an image cluster can be identified by assessing the products of greyscale intensity (I_k) and pixel distance in x (x_{n_k}) for each pixel within the assessment region (N), summing the results, and dividing by the sum of all pixel intensities.

By assuming the standard deviation in greyscale intensity is fairly spread throughout the image, Equation 22 can be altered to Equation 23, allowing theoretical prediction of the error in centroid location for any speckle group.

$$\Delta x_{n_c} \approx x_{n_k} - \frac{N x_{n_k} (I_m + \sigma)}{N I_m} \quad (23)$$

This suggests an approximation of error (Δx_{n_c}) in locating the cluster center can be

calculated using the number of pixels in the area (N), the expected center (x_{n_k}), mean intensity of the image (I_m), and standard deviation (σ) of pixel greyscale fluctuation.

Our DIC assessment used a subset size of 39 pixels; therefore, the number of pixels in the subset (N) is 1521, and the expected centroid position (x_{n_k}) is 19. With an average greyscale value of the original image (Figure 14a) as 55.72, we find Δx_{n_c} to be 0.425 pixels.

As the subset is square, this value is the same for the centroid location in the "y" orientation. In other words, $\Delta y_{n_c} = \Delta x_{n_c} = 0.425 \text{ pixels}$. By using the values calculated, in combination with Pythagoras theorem, we find the absolute difference in centroid position, for each centroid assessed (i.e. end points of the virtual strain gauge), to be:

$$\Delta \text{abs}_{n_c} = \sqrt{\Delta x_{n_c}^2 + \Delta y_{n_c}^2} = 0.602 \text{ pixels} \quad (24)$$

Thus, the error in strain estimation based on the inaccuracies of the gauge end point locations is:

$$\text{Error\%} = 100 \cdot \frac{\Delta \text{abs}_{n_c}}{L_{VSG}} = \frac{0.602 \text{ pixels}}{99 \text{ pixels}} \cdot 100 \% = 0.608 \% \quad (25)$$

This value is 0.608% the length of the virtual strain gauge used in DIC assessment is an error on 1D distance measurement. Since two cameras are used in the experiments to compute all strain components, the error in experimental strain measurements due to imaging capabilities is estimated as $2 \cdot 0.608\% = 1.216\%$.

4.3.2. Sensitivity of our algorithm to random, experimental noise

In order to assess the impact of measurement noise level on the robustness of the proposed algorithm, we applied a stochastic noise on the strain maps supplied as input into our algorithm. We added a normal distribution of strain values with the mean value of $1.25\% \cdot \max(\epsilon_{axial})$. Stochastic noise distributions and their effect on the strain data used as the input are shown in Figure 15.

Case with perturbed strain input values converges from the uniform strain distribution to the experimental values, even though the algorithm updates material properties in each iteration. Achieving strain convergence in the numerical models is a good indicator that the model's stress and material properties match the values in the experimental/virtual experiment component.

Young modulus and Poisson ratio distribution converge to stable configurations, which resemble the virtual component's material fields. The errors imposed on three strain components of 1.25 % appear to accumulate to $3 \cdot 1.25\% \approx 5 - 7\%$ observed in Figure 17. Application of the 3 points Gaussian filter reduced the noise of the algorithmic result. The use of a Gaussian filter is a common practice in the post-processing of digital correlation results. It might be a useful technique to treat and reduce the impact of the experimental noise in the proposed iterative algorithm.

4.4. Discussion

The proposed algorithm does not use a global cost function. Conversely, our approach employs constitutive, material relations at the element level, where measured strains (as-

sumed to be true) and simulated stress values are used to update the material constants from iteration to iteration. The approach stiffens and softens the elastic constants depending on the differences between the simulated and measured strain values. The algorithm produced stable stress and material field solutions for a range of 2D and 3D benchmark cases. The algorithm is sensitive to the rate of spatial variations and cross-correlations between the variables, with slower convergence for the cases with more abrupt changes of material properties between neighbouring elements. The addition of random noise (to simulate experimental and imaging inaccuracies) reduced the precision of the computed material fields. At the same time, the algorithm converged rapidly and produced reasonably accurate results for engineering applications. The application of a 3pts Gaussian filter reduced the experimental noise's impact on the results and is recommended for processing of real-life experimental data. Although we demonstrated the robustness and accuracy of PB-FEUM through virtual experimentation, further studies shall apply the methodology to true experimental data from FFMT.

PB-FEUM can also contribute to stochastic-process modeling research fields where Young's modulus and Poisson's ratio are represented as stochastic fields instead of deterministic values. Cross-correlation between material variables and spatial (distance related) correlations could be estimated from material parameter fields computed using PB-FEUM. These stochastic parameters are known as kernels (depicted in eq. 19). Experiment-based representation of material variation as stochastic fields (with spatial correlation and cross-correlation between the variables) allows a range of engineering disciplines to develop a better probabilistic understanding of heterogeneous materials. Such parametric representation, employing fitted analytical kernel functions to the experiment-based discrete material field data, is beyond the scope of this paper and requires further research.

Mathematically speaking our method is similar in its spirit to iterative methods for solving systems of linear equations. In these methods, a guess of the variables is a starting point (in our case, average values). Each iteration employs the system of equations to compute the new values and put these new values in the original system of equations for the next iterations. Chapter 5 of Modern Engineering Mathematics by James Glyn [33] gives numerical examples, which illustrate this approach. When all variables are updated at once, it is called the Jacobi method, and when variables are updated as soon as they are calculated, it is called the Gauss-Seidel method. Interestingly, successive over-relaxation (SOR) speeds up the iterative method. It anticipates what the x_i values might be. It overshoots the values, where each new value is the weighted average of the previous value and the new value, with a range of allowed weighting coefficients, w selected for various numerical problems. Our method updates the stress values first and material properties in the next sub-step, and thus it has a sequential nature. Therefore, it resembles the Gauss-Seidel approach, where variables are updated as soon as they are available. Our sequence is systematic because stress values are updated first and material property subset next.

In essence, material variables are embedded in element stiffness matrices, which are assembled into the global stiffness matrix of the finite element solver. Thus, our system of equations is the product of the global stiffness matrix and displacement, with external nodal forces on the right-hand side. The unknown variables are material properties and

displacements, which are related to strains. We introduced additional equations, which link the material variables with the measured strains via constitutive relationships because the measured strains are additional pieces of information. Thus, we overloaded stress-strain relationships to employ additional information about the strain field from the test. Thereby, our approach is consistent with the Gauss-Seidel method because we pass variables from a subset of linear equations, namely finite element mechanical solver, to the other system of equations, consisting of measured strain, material parameters and simulated stress. Generally speaking, overloading certain equations with experimental information appears to be an effective way to iteratively solve inverse problems, focusing on adjusting parameters to match experimentally measured data.

Typically, the Gauss-Seidel method is slowly converging and requires 20 or more iterations to reach high precision. We have seen rapid convergence to within several % of the benchmark solution, but later the convergence slows down noticeably. Considerable mathematical knowledge is needed to postulate, develop and prove the convergence criteria. One simple check is to test whether a matrix is diagonally dominant. That means that the magnitude of a diagonal element is larger than the sum of the off-diagonal elements in that row, for all rows. Finite element analysis of stress and strains is known to produce diagonally dominant global stiffness and mass matrices, which might hint that the inverse problem studied here is suitable for application of the iterative methods. Generally speaking, a detailed analysis of the convergence is not possible without studying eigenvalues [33] and is beyond the scope of this paper. Excellent treatment of iterative methods and convergence analysis can be found in Applied Linear Algebra by Olver and Shakidan [34].

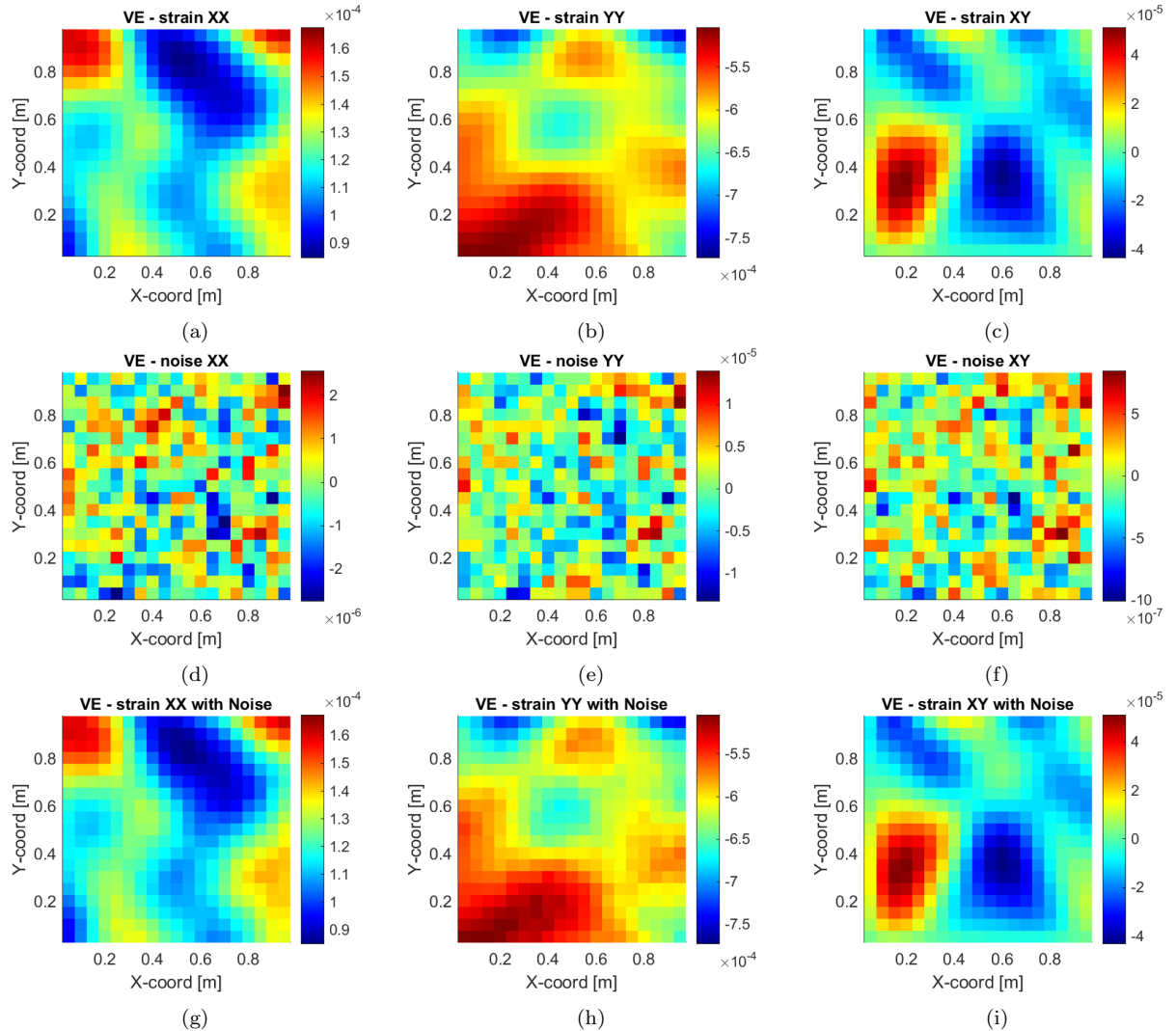


Figure 15: Stochastic noise was applied to the strains from the virtual experiment to assess the impact of imaging and experimental inaccuracies. (a-c) Idealized strains from the virtual experiment, (d-f) random strains corresponding to feasible measurement noise levels, (g-i) strain fields consisting of the baseline strains with added random, stochastic noise.

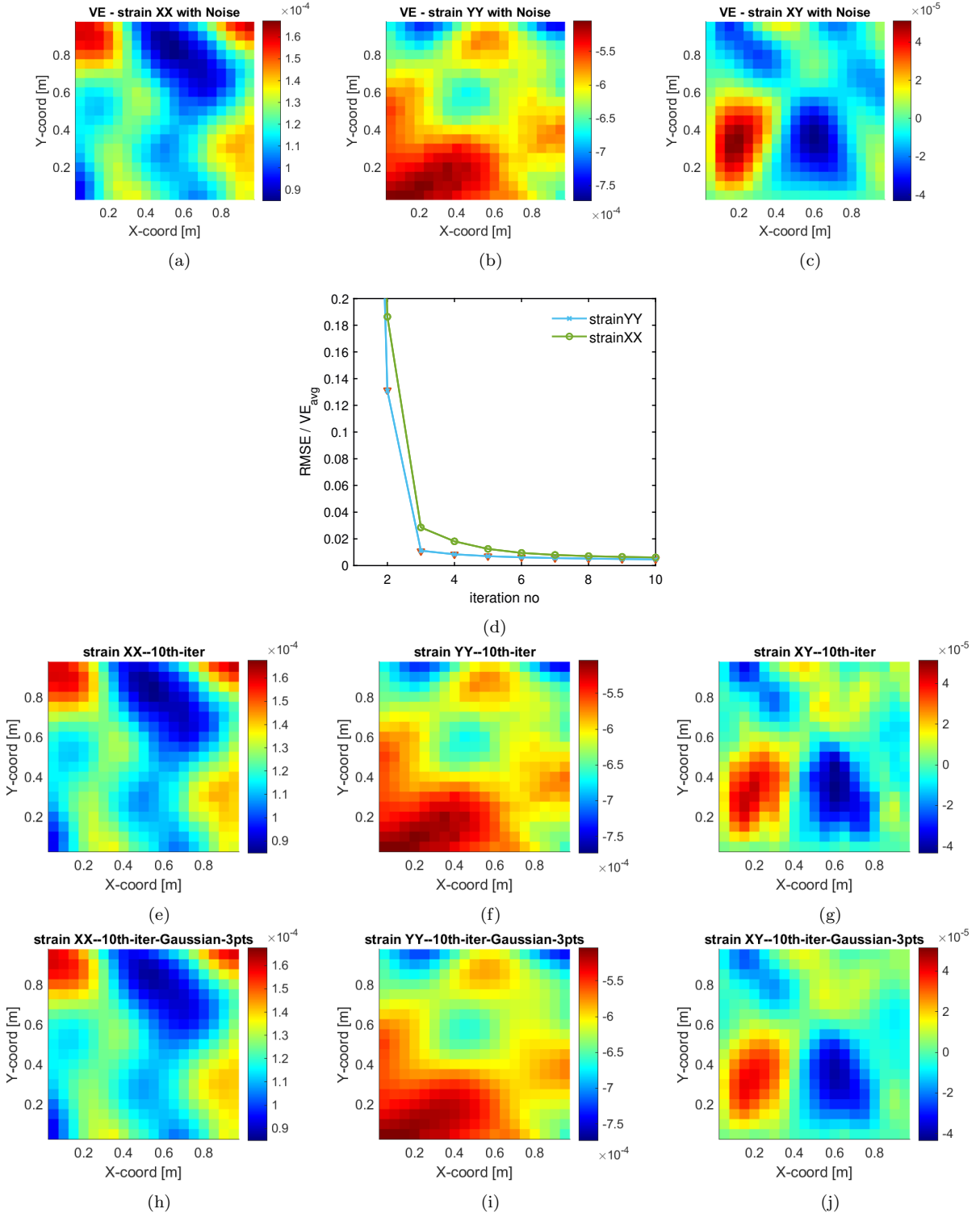


Figure 16: Convergence of the computed strain fields compared to the input fields. (a-c) Strains from virtual experiment (VE). (d) Root mean square error (RMSE) is decreasing rapidly. (e-g) Converged strain results produced by our algorithm, which started from the uniform strain distribution. (h-j) Converged strains after application of 3 points Gaussian filter to reduce the random noise.

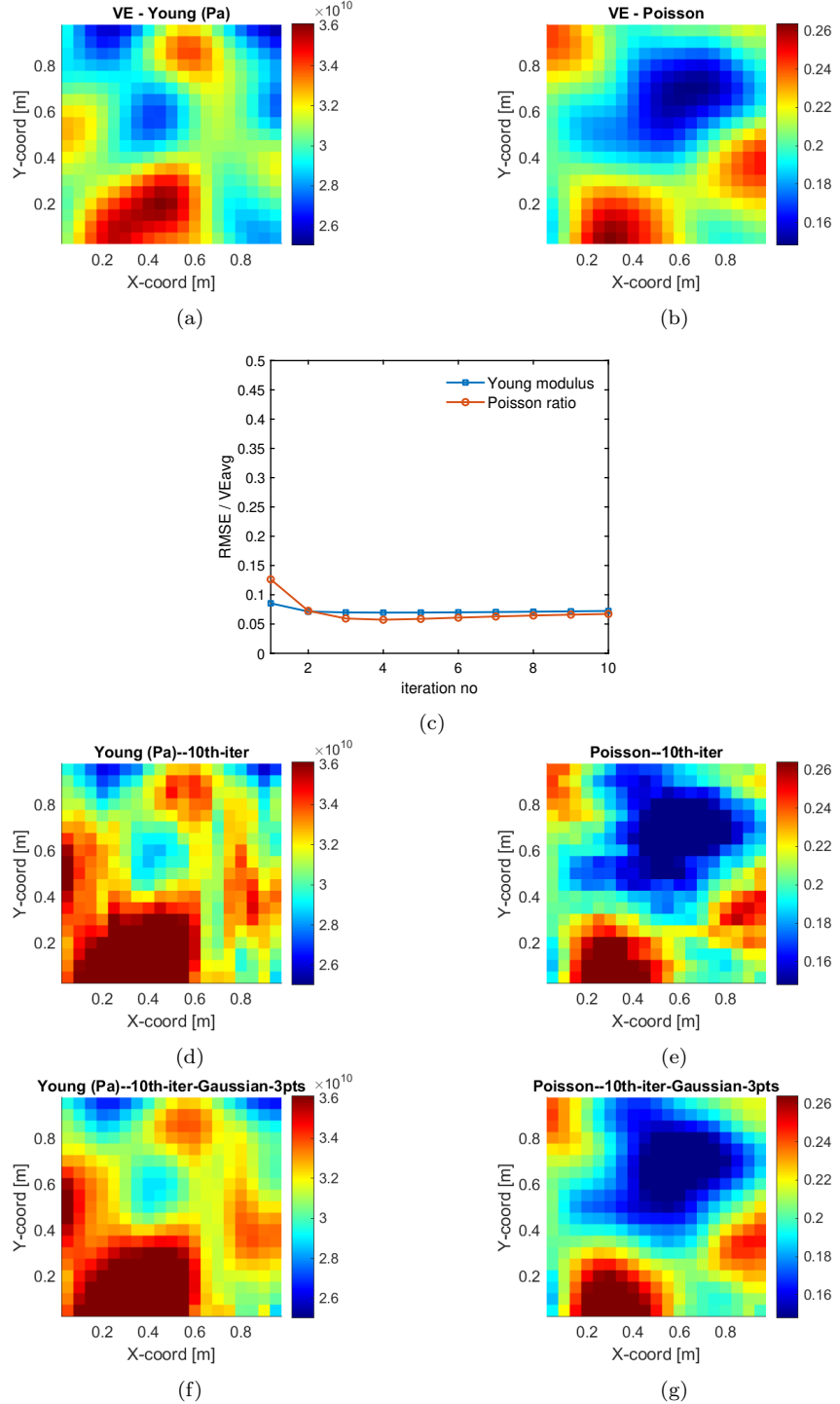


Figure 17: Convergence of elastic constants. (a-b) Given input values from the virtual experiment (VE) benchmark problem. (c) Convergence of the normalized root mean square error demonstrates that material properties approach the true values. Experimental noise from three strain fields seems to accumulate in the computations of material elastic constants. (d-e) The converged material properties produced by our algorithm resemble the benchmark values. (f-g) Application of three point Gaussian filter to the converged results reduced the impact of the experimental measurement noise.

5. Conclusion

This study introduced a novel physics-based (PB) algorithm for computing spatially varying material properties based on the full-field strain measurements for 2D and 3D cases. The proposed algorithm used physical relationships between the strains and stresses to update the material constants, where measured strains were kept constant, and stress values were updated in each iteration. The application of the proposed iterative algorithm resulted in the stiffening of the material in locations with overestimated computational strain and softening in the regions with underestimated computational strains. The proposed method reached satisfactory results after only several iterations and updating required linear evaluations only. Since the iterations are performed on the element basis, the algorithm lends itself to parallelization (e.g. through the use of multiple processors in *for* loops).

Virtual Experiments (VEs) were employed to test the algorithm under a wide range of scenarios. Spatially correlated functions were used to ensure heterogeneity and discontinuities in the material fields, which generated a high-quality suite of benchmark cases. Satisfactory convergence was obtained for all cases (2D and 3D) for both elastic constants, namely Young modulus and Poisson ratio, reaching errors lower than 5% in all cases. The algorithm was effective under multi-axial stress states (corresponding to 2D and 3D dimensional fields), where the stresses and strains were redistributed between the elements, and noticeable local shear deformations took place. Thus, the stochastic benchmark tests demonstrated the suitability of the proposed PB-FEUM approach for computing spatial distributions of material properties from the given full-field strain fields, the externally applied load, and average values of Young's modulus and Poisson's ratio to start the iterations. In summary, the proposed method enables the identification of spatially varying mechanical properties using full-field measurement techniques, such as digital image correlation or digital volume correlation.

We estimated strain measurement error based on the variation of greyscales between two images of the unloaded specimen. The conservative error estimation of 1.25% of the maximum strain was applied to three measured strain components independently. Iterative algorithm converged to the supplied strain field values. The introduced measurement error propagated cumulatively, resulting in an overall accuracy of approximately 7%. The application of 3 points Gaussian filter, which is a standard technique of treating noise in field measurements, improved the quality of the computed results.

Regarding future directions, the application of PB-FEUM to other material types, such as elasto-viscoplastic materials, shall be explored. Multi-step loading and different types of loading conditions, e.g. dynamic loading, could be considered in the future. Multi-step loading might produce piecewise linear material parameters, while the dynamic tests will require the inclusion of inertia in the simulations employed for finite element updating. Future research shall extend PB-FEUM to samples and components with discontinuities such as rocks with natural voids or steel foam with macroscopic voids and porosities.

Acknowledgements

The authors would like to express heartfelt gratitude to our academic colleagues for their feedback and fruitful discussions. We also would like to express our gratitude to technicians who assisted us during the mechanical tests, namely Mr Peter Heynes and David Jesson.

This study was funded by the Research Framework of the European Commission under METFOAM Career Integration Grant 631827 with support from program manager Dr. Ing. Antonio Cipollaro. The work was also supported by the impact acceleration grant no EP/P511456/1, provided by the Engineering and Physical Science Council (EPSRC) in the UK. Support of Dr. Sue Angulatta, a local program manager, is genuinely appreciated. Luiz C.M. Vieira Jr. is indebted to the Brazilian National Council for Scientific and Technological Development (CNPq) for the research productivity fellowship grant 304005/2017-7. Any opinions, findings, and conclusions expressed in this article are those of the author(s) and do not necessarily reflect the views of EPSRC, the Brazilian National Council for Scientific and Technological Development (CNPq) or the European Commission.

Nomenclature

β	Cross-correlation magnitude
ε^*	Experimental strain tensor
ε	Strain tensor
n	Normal vector on the boundary
Δ	Coefficient of variation
Δ_ν	Poisson's ratio coefficient of variation
Δ_E	Young's modulus coefficient of variation
γ	Correlation length or scale of fluctuation
σ	Stress tensor
\mathbf{b}	Vector of body forces
\mathbf{C}	Stiffness tensor
\mathbf{x}	Element centroid coordinate
v	Variable of interest
v_{VE}	Virtual Experiment variables
μ_ν	Poisson's ratio average value

μ_E	Young's modulus average value
ν	Poisson's ratio
Φ	Gaussian random and correlated variable
ϕ	Gaussian random and uncorrelated variable
E	Young's modulus
K	Correlation matrix
k	Squared Exponential covariance function
R	Matrix of distance between each pair of elements
S	Singular values of matrix K
std_E	Young's modulus standard deviation
std_{ν}	Poisson's ratio standard deviation
U	Left singular vector of matrix K
V	Right singular vector of matrix K
m	Elements number
VE	Virtual Experiment

References

- [1] S. Torquato, Random Heterogeneous Materials: Microstructure and Macroscopic Properties, Interdisciplinary Applied Mathematics, Springer New York, 2013.
URL <https://books.google.com.br/books?id=UTfoBwAAQBAJ>
- [2] P. Pollock, L. Yu, M. Sutton, S. Guo, P. Majumdar, M. Gresil, Full-field measurements for determining orthotropic elastic parameters of woven glass-epoxy composites using off-axis tensile specimens, *Experimental Techniques* 38 (4) (2014) 61–71. arXiv:<https://onlinelibrary.wiley.com/doi/pdf/10.1111/j.1747-1567.2012.00824.x>. doi:[10.1111/j.1747-1567.2012.00824.x](https://doi.org/10.1111/j.1747-1567.2012.00824.x)
- [3] J. H. Lee, T. Kim, H. Lee, A study on robust indentation techniques to evaluate elastic-plastic properties of metals, *International Journal of Solids and Structures* 47 (5) (2010) 647–664.
- [4] J. J. Kim, T.-H. Pham, S.-E. Kim, Instrumented indentation testing and fe analysis for investigation of mechanical properties in structural steel weld zone, *International Journal of Mechanical Sciences* 103 (2015) 265–274.
- [5] J. Phadikar, T. Bogetti, A. M. Karlsson, On the uniqueness and sensitivity of indentation testing of isotropic materials, *International journal of solids and structures* 50 (20-21) (2013) 3242–3253.
- [6] K.-H. Chung, W. Lee, J. H. Kim, C. Kim, S. H. Park, D. Kwon, K. Chung, Characterization of mechanical properties by indentation tests and fe analysis-validation by application to a weld zone of dp590 steel, *International Journal of Solids and Structures* 46 (2) (2009) 344–363.
- [7] D. M. De Bono, T. London, M. Baker, M. J. Whiting, A robust inverse analysis method to estimate the local tensile properties of heterogeneous materials from nano-indentation data, *International Journal of Mechanical Sciences* 123 (2017) 162–176.
- [8] F. Pierron, M. Grédiac, The Virtual Fields Method: Extracting Constitutive Mechanical Parameters from Full-field Deformation Measurements, Springer New York, 2012.
URL <https://books.google.com.br/books?id=GGGQ60VLSc8C>
- [9] N. McCormick, J. Lord, Digital Image Correlation, *Materials Today* 13 (12) (2010) 52–54. doi:[https://doi.org/10.1016/S1369-7021\(10\)70235-2](https://doi.org/10.1016/S1369-7021(10)70235-2).
- [10] B. K. Bay, T. Smith, D. P. F. et al, Digital volume correlation: Three-dimensional strain mapping using X-ray tomography, *Experimental Mechanics* 39 (1999) 217. doi:<https://doi.org/10.1007/BF02323555>.
- [11] B. C. Roberts, E. Perilli, K. J. Reynolds, Application of the digital volume correlation technique for the measurement of displacement and strain fields in bone: A literature review, *Journal of Biomechanics* 47 (5) (2014) 923–934. doi:<https://doi.org/10.1016/j.jbiomech.2014.01.001>.
URL <http://www.sciencedirect.com/science/article/pii/S0021929014000037>
- [12] B. K. Bay, Methods and applications of digital volume correlation, *The Journal of Strain Analysis for Engineering Design* 43 (8) (2008) 745–760. doi:<https://doi.org/10.1243/03093247JSA436>.
- [13] L. Petureau, P. Doumalin, F. Bremand, Identification of Local Elastic Parameters in Heterogeneous Materials Using a Parallelized Femu Method, *International Journal of Applied Mechanics and Engineering* 24 (4) (2019) 140–156. doi:[10.2478/ijame-2019-0054](https://doi.org/10.2478/ijame-2019-0054).
URL <https://content.sciendo.com/view/journals/ijame/24/4/article-p140.xml>
- [14] S. Huang, P. Feissel, P. Villon, Modified constitutive relation error: An identification framework dealing with the reliability of information, *Computer Methods in Applied Mechanics and Engineering* 311 (2016) 1–17. doi:[10.1016/j.cma.2016.06.030](https://doi.org/10.1016/j.cma.2016.06.030).
URL <https://www.sciencedirect.com/science/article/pii/S0045782516306557>
- [15] U. Albocher, P. E. Barbone, A. A. Oberai, I. Harari, Uniqueness of inverse problems of isotropic incompressible three-dimensional elasticity, *Journal of the Mechanics and Physics of Solids* 73 (2014) 55–68. doi:[10.1016/j.jmps.2014.08.010](https://doi.org/10.1016/j.jmps.2014.08.010).
URL <https://www.sciencedirect.com/science/article/pii/S002250961400177X>
- [16] B. Rahmani, F. Mortazavi, I. Villemure, M. Levesque, A new approach to inverse identification of mechanical properties of composite materials: Regularized model updating, *Composite Structures* 105 (2013) 116–125. doi:[10.1016/j.compstruct.2013.04.025](https://doi.org/10.1016/j.compstruct.2013.04.025).
URL <https://www.sciencedirect.com/science/article/pii/S0263822313001773>

- [17] F. Latourte, A. Chrysochoos, S. Pagano, B. Wattrisse, Elastoplastic Behavior Identification for Heterogeneous Loadings and Materials, *Experimental Mechanics* 48 (4) (2008) 435–449. doi:10.1007/s11340-007-9088-y.
 URL <http://link.springer.com/10.1007/s11340-007-9088-y>
- [18] T. Merzouki, H. Nouri, F. Roger, Direct identification of nonlinear damage behavior of composite materials using the constitutive equation gap method, *International Journal of Mechanical Sciences* 89 (2014) 487–499. doi:10.1016/j.ijmecsci.2014.10.002.
 URL <https://www.sciencedirect.com/science/article/pii/S0020740314003233>
- [19] E. Florentin, G. Lubineau, Identification of the parameters of an elastic material model using the constitutive equation gap method, *Computational Mechanics* 46 (4) (2010) 521–531. doi:10.1007/s00466-010-0496-y.
 URL <https://doi.org/10.1007/s00466-010-0496-y>
- [20] D. Claire, F. Hild, S. Roux, A finite element formulation to identify damage fields: the equilibrium gap method, *International Journal for Numerical Methods in Engineering* 61 (2) (2004) 189–208. doi:<https://doi.org/10.1002/nme.1057>.
 URL <https://onlinelibrary.wiley.com/doi/abs/10.1002/nme.1057>
- [21] J. Réthoré, S. Roux, F. Hild, An extended and integrated digital image correlation technique applied to the analysis of fractured samples, *European Journal of Computational Mechanics* 18 (3-4) (2009) 285–306. doi:10.3166/ejcm.18.285-306.
 URL <https://doi.org/10.3166/ejcm.18.285-306>
- [22] H. D. Bui, A. Constantinescu, H. Maigre, Numerical identification of linear cracks in 2D elastodynamics using the instantaneous reciprocity gap, *Inverse Problems* 20 (4) (2004) 993–1001. doi:10.1088/0266-5611/20/4/001.
 URL <https://iopscience.iop.org/article/10.1088/0266-5611/20/4/001>
- [23] N. Auffray, M. Bonnet, S. Pagano, Identification of transient heat sources using the reciprocity gap, *Inverse Problems in Science and Engineering* 21 (4) (2013) 721–738. doi:10.1080/17415977.2012.731597.
 URL <https://doi.org/10.1080/17415977.2012.731597>
- [24] L. Zhang, S. G. Thakku, M. R. Beotra, M. Baskaran, T. Aung, J. C. H. Goh, N. G. Strouthidis, M. J. A. Girard, Verification of a virtual fields method to extract the mechanical properties of human optic nerve head tissues in vivo, *Biomechanics and Modeling in Mechanobiology* 16 (3) (2017) 871–887. doi:10.1007/s10237-016-0858-2.
 URL <http://link.springer.com/10.1007/s10237-016-0858-2>
- [25] J. Martins, A. Andrade-Campos, S. Thuillier, Comparison of inverse identification strategies for constitutive mechanical models using full-field measurements, *International Journal of Mechanical Sciences* 145 (2018) 330–345. doi:10.1016/j.ijmecsci.2018.07.013.
 URL <https://linkinghub.elsevier.com/retrieve/pii/S0020740318305836>
- [26] M. Grediac, F. Pierron, S. Avril, E. Toussaint, The Virtual Fields Method for Extracting Constitutive Parameters From Full-Field Measurements: a Review, *Strain* 42 (4) (2006) 233–253. doi:<http://10.1111/j.1475-1305.2006.tb01504.x>.
 URL <https://onlinelibrary.wiley.com/doi/abs/10.1111/j.1475-1305.2006.tb01504.x>
- [27] S. Avril, F. Pierron, General framework for the identification of constitutive parameters from full-field measurements in linear elasticity, *International Journal of Solids and Structures* 44 (14–15) (2006) 4978–5002. doi:<http://10.1016/j.ijsolstr.2006.12.018>.
- [28] D. J. DeGroot, G. B. Baecher, Estimating autocovariance of in-situ soil properties, *Journal of Geotechnical Engineering* 119 (1) (1993) 147–166.
- [29] P. G. Cranston, M. C. Richie, L. C. V. Jr., Effects of soil support on the stability of corrugated metal pipe., in: Structural Stability Research Council - Annual Stability Conference, 2017.
- [30] P. Lava, S. Cooreman, S. Coppieters, M. De Strycker, D. Debruyne, Assessment of measuring errors in DIC using deformation fields generated by plastic FEA, *Optics and Lasers in Engineering* 47 (7-8) (2009) 747–753. doi:10.1016/j.optlaseng.2009.03.007.
 URL <https://linkinghub.elsevier.com/retrieve/pii/S0143816609000451>

- [31] M. Rossi, P. Lava, F. Pierron, D. Debruyne, M. Sasso, Effect of DIC Spatial Resolution, Noise and Interpolation Error on Identification Results with the VFM, *Strain* 51 (3) (2015) 206–222. doi:<http://10.1111/str.12134>.
- [32] V. Naidu, G. G., J. R. Raol, Data fusion for identity estimation and tracking of centroid using imaging sensor data, *Defence Science Journal* 57 (5) (2007) 639–652. doi:[10.14429/dsj.57.1797](https://doi.org/10.14429/dsj.57.1797)
URL <http://publications.drdo.gov.in/ojs/index.php/dsj/article/view/1797>
- [33] G. James, Modern engineering mathematics, fifth edition Edition, Prentice Hall, Harlow, England, 2015.
- [34] P. J. Olver, C. Shakiban, Applied Linear Algebra, 2nd Edition, Undergraduate Texts in Mathematics, Springer International Publishing, 2018. doi:[10.1007/978-3-319-91041-3](https://doi.org/10.1007/978-3-319-91041-3)
URL <https://www.springer.com/gp/book/9783319910406>